Finite element modeling of steady plastic shockwaves in porous metals: Role of size, shape, and spatial distribution of voids

Eyass Massarwa, Christophe Czarnota, Alain Molinari

Finite Element Modeling of steady plastic shockwaves in porous metals: Role of size, shape, and spatial distribution of voids

Eyass Massarwa[1,2], Christophe Czarnota[1,2], and Alain Molinari [1,2,*]

[1] Laboratoire d'Etude des Microstructures et de Mécanique des Matériaux (LEM3), CNRS, Université de Lorraine, Arts & Métiers ParisTech, F-57000 Metz, France

[2] Laboratory of Excellence on Design of Alloy Metals for low-mAss Structures (DAMAS), Université de Lorraine, 57000 Metz, France

Abstract

This paper aims at developing a finite-element model, which simulates a planar impact experiment on a ductile metallic porous material. When the shockwave passes through a porous medium, the voids face a rapid collapse, and the material particles in the vicinity of the voids are subjected to very high acceleration. Acceleration forces generated at the microscale level may affect the overall response of the porous material. Analyzing the effect of the initial porosity, size, shape, and spatial distribution of voids on the plastic shock velocity and the shock structure was the main objective of this work. It is found that, for a given impact velocity, the plastic shock velocity depends solely on the material parameters of the dense material and the initial porosity. However, the size, shape and spatial distribution of voids, together with the initial porosity, play a significant role on the structure of the plastic shock.

Keywords: Planar plastic shock waves, porous metals, FE modeling, shock speed, shock structure, effect of void configuration.

corresponding author: alain.molinari@univ-lorraine.fr *

1. Introduction

Porous metals are attractive materials for a wide range of engineering and scientific applications where energy absorption is critical. This includes the design of materials for body armors and shock-mitigating structures in a variety of sectors, from aerospace and defense to maritime and automotive industries [1-7]. Porosities may be the result of defects or can be created and regulated for engineering performance and a particular function. In this regard, the recent development of additive manufacturing technologies provides targeted and controlled pore distributions with specific void sizes and shapes in an attempt to generate an optimal material design for security purposes [8-9]. This tailoring of the internal structure can be relevant for optimizing porous structures under shock loading.

Among various shockwave characteristics, the shock width appears as a critical parameter in the shock response of materials since it relates to the severity of the shockwave. More specifically, by spreading the shock layer width, one is able to reduce the accelerations sustained by material particles and consequently mitigate some of the adverse effects driven by a strong impact [10]. The objectives of the present work seek to utilize finite element calculations in order to elucidate the influence of size, shape, and spatial distribution of pores on steady shock wave propagation and plastic shock width. The effect of initial porosity and impact speed will be examined as well. The paper thereby provides new insights that are important for designing porous materials to mitigate the effects of shockwaves.

Under rapid loading, such as in plate impact experiments, a fast void collapse occurs when the plastic shock wave sweeps through voids. This gives rise to a large acceleration of material particles in the vicinity of the voids. These local acceleration forces, which are referred to as micro-inertia effects, may play a crucial role in the macroscopic material response. In fact, for spherical voids, the initial radius turns out as a natural length scale which strongly influences the overall dynamic response of the material. This was illustrated in several problems, like spall

fracture [11-14], dynamic cracking [15-16], or shock propagation in cellular and porous solids [10, 17-19]. Size effects (which are naturally involved in micro-inertia dependent approaches) also emerge from strain gradient plasticity models. This was illustrated by dos Santos et al. [20] in a study of dynamic expansion of a spherical cavity in a homogenized porous medium. Note however that the material intrinsic length scale introduced in nonlocal continuum plasticity models has its source in a very different kind of physics (e.g. grain size and geometrically necessary dislocations). In addition, the vanishing of the length scale effect, which is observed at low strain rates in micro-inertia dependent models, does not occur in strain gradient plasticity. Czarnota et al., [10] proposed a micro-inertia dependent model based on the dynamic homogenization approach of Molinari and Mercier [21]. For a given shock stress amplitude, and for large enough initial voids, it was shown that the shock layer width in porous aluminum may be larger than in dense aluminum. Recently, the experimental work conducted by Lovinger et al. [22] on closed-cell porous aluminum, has provided evidence of micro-inertia's effect on shock response.

It turns out, in some circumstances depending on the porous microstructure, loading rates, and matrix behavior, that the dynamic response may be largely or slightly influenced by micro-inertia. The analysis of steady plastic shockwaves conducted by Czarnota et al. [18], has revealed the existence of two extreme regimes governing the structure of plastic shocks: a viscous dominated regime (where the initial void radius has no effect on results) prevailing at low shock pressure and a micro-inertia dominated regime holding at sufficiently large amplitude shocks. In this latter case, the shock layer width is found scaled by the initial void radius. In another study case, where strain rates are much lower than in shock experiments, Nieto-Fuentes et al. [23] showed from finite element calculations performed with and without the microinertia-based model of Jacques et al., [15], that microinertia does not affect the dynamic formability of porous sheet specimens (at least before necking).

Note that theoretical and numerical approaches cited above considered voids of initial spherical shape. In many cases, porous materials contain pores with various initial sizes, shapes and spatial distributions. Under high strain rates loading, micro-inertia effects were shown not only to depend on the porosity and void size (e.g. see analytical approaches for unit cell calculations in [21, 24-25] for spherical voids) but also on the shape (see Sartori et al. [26-27] for spheroidal; Subramani et al. [28] for cylindrical voids). However, only a few studies have examined more than just the size effect in dynamic problems. The effect of the initial void shape was recently examined by dos Santos et al. [29]. In this work, the size effects, which would have been brought by micro-inertia or strain-gradient plasticity, were ignored. The cavity was expanding in a homogenized porous domain described with the static yield criterion of Monchiet et al. [30] developed for spheroidal voids embedded into an orthotropic matrix. It was shown that oblate voids prevent shock formation while prolate and spherical voids displayed a sudden drop in stresses which is a signature of the formation of a shock.

One subject related to the dynamics of porous materials is the interaction of a single void or an array of voids collapsing after the passage of a stress wave. This has led to numerous investigations based on calculations conducted at the atomistic and nanometer scales (e.g. [31-36]). Some other numerical works tracked the shock response of porous materials at the continuum scale using Molecular Dynamics (MD) (e.g. [37-38]), hydrocodes (e.g. [33]) or Arbitrary-Lagrangian- Eulerian Finite Element (FE) calculations (e.g. [39-42]). Most studies focused on hot-spot formation (which is known to be the primary mechanism for detonation initiation) in energetic materials, dislocation loops emission, and collapse mechanisms in various materials.

From two- or three-dimensional based calculations, the size effect was investigated considering circular or spherical voids [32, 34, 37-40]. However, as previously mentioned, the focus was

on collapse mechanisms in porous materials under shock loading. Moreover, the genuine effect of the void size was not clearly reported.

Simulations of a single pore of size ranging from 10nm to 10µm were conducted by Wood et al. [33] at the mesoscale using a shock physics hydrocode including Steinberg-Guinan-Lund (SGL) strain rate dependent strength model. They showed, for a given cell, that an increase in the void radius leads to an increase in the void collapse rate. However, this counter-intuitive influence of micro-inertia effects should be interpreted with care. In fact, the porosity was altered when modifying the pore radius, such that the influence of the void size was not isolated. Such examination of the size effect, i.e. the porosity varying with the void radius, was also considered in the recent work of Sharma and Durbey [36] who focused on the shock and spall response of single aluminum crystal. The genuine effect of the void size was not captured.

Few efforts have been dedicated so far to incorporate the void shape effect. Zhao et al. [31] performed two-dimensional large-scale MD simulations to study the effect of the microstructure featured by pore shape, arrangement, and size, as well as grain boundaries on void collapse mechanisms in high porosity copper nanofoams under shock loading. Elliptical voids with large aspect ratios, and with the major axis parallel to the shock wave direction, were shown to yield high speed jetting and vaporization. This finding is in line with [41], within the context of hot spot formation in energetic materials, for which the void having its major axis aligned with the wave propagation direction was shown to promote the formation of a faster jet, and a larger hotspot. More recently, Song et al. [35] examined via three-dimensional MD simulations, the shock response of nanoporous metallic glasses. They considered three configurations of a longitudinal 3D bar, each containing three identical voids (spherical and prolate voids aligned with and perpendicular to the wave propagation direction). The effect of void shape was shown to depend on the shock amplitude. Recent works focused on the application of machine learning methods to elucidate the role of shape and arrangement of voids

in shock wave loadings. In [43], ANN (Artificial Neuron Network) and a micromechanical model were used to examine, using MD, unit cells containing a single void with various shapes (spherical, cubic, cylindrical). The micromechanical modeling developed by the authors considers voids of various shapes but the mass density and related inertia were not included, which can be justified at this nanoscale. Indeed, it was shown in previous studies [10, 44] that micro-inertia is substantial for micrometer-size pores but negligible for nanopores. From simulations of the propagation of a shockwave in a nanoporous aluminum, they concluded that the specific shape influences only some details of the shock wave propagation, while the structure is close for all considered pore shapes. It will be shown in our work that the shape of voids may play an important role in porous aluminum containing bigger voids.

In addition to calculations considering a single void or a specific pattern of voids, some works accounted for an explicit description of the void population, e.g. to mimic real microstructures of voided materials. This has been previously illustrated when referring to several dynamic problems examined in the literature where microstructures with spherical voids were built to match experimentally observed microstructures (e.g. Wood et al. [33], Nieto-Fuentes et al. [23], Vishnu et al. [45]).

Although there have been numerous studies on the shock response of porous materials, to the best of the authors' knowledge, the present research devoted to elucidating the role of initial porosity and void configuration (i.e. void shape, size, and spatial distribution) on the plastic shock structure and speed has not been reported elsewhere. MD simulations still are the most common approaches to investigate the pore effects. Thus, a large number of numerical simulations were conducted at time and length scales far below the continuum mesoscale. Moreover, analyzing the shock wave in steady-state propagation was not the fundamental concern in investigations reported in the literature. In fact, reaching steady state in wave propagation requires a sufficiently large domain within which the wave needs some distance to

balance nonlinear steepening effects with dissipative smoothing effects. During the unsteady propagation, both the shock structure and the void closure mechanism evolve [38].

The paper is organized as follows. In Section 2, the FE model demonstrating a porous long bar under a planar impact condition is developed. The constitutive modeling of ductile aluminum, adopted as the matrix material surrounding voids, is also presented. In Section 3 the calibration of the material parameters using experimental plastic shock profiles of dense aluminum available in the literature is proposed including a comparison of $U_s - U_p$ diagram for dense aluminum obtained by experiments and by the FE model. Next, a dimensional analysis, providing a functional relationship relating independent dimensional parameters considered in the FE modeling, is proposed in Section 4. The characterization of the shock width is also detailed in Section 4. Finally, in section 5, the effects of the size, shape and spatial distribution of voids on steady plastic shocks is elucidated.

2. Methods

In the present study, the shock compaction response of a porous ductile medium is analyzed using the finite-element (FE) software Abaqus/Explicit. We developed a two-dimensional axisymmetric FE model, representing a long cylindrical bar with initial porosity and impacted by a rigid body. Herein, it is assumed that a porous sample subjected to a planar impact experiment can be idealized through the plate thickness by a representative bar with a circular cross-section, subjected macroscopically to uniaxial deformation. This cylinder contains spheroidal voids homogeneously distributed along the center line of the bar. The mechanical response of the ductile metallic matrix material is defined using the Cowper-Symonds model (Cowper & Symonds [46]) and the Mie-Grüneisen equation of state (EOS) (Meyers [47]).

2.1 2D Axisymmetric Cylindrical RVE

To analyze the dynamic response of the porous medium with the FE numerical tool, a microscale 2D axisymmetric cylindrical computational RVE model can be used to represent the microstructural configuration, Fig.1.

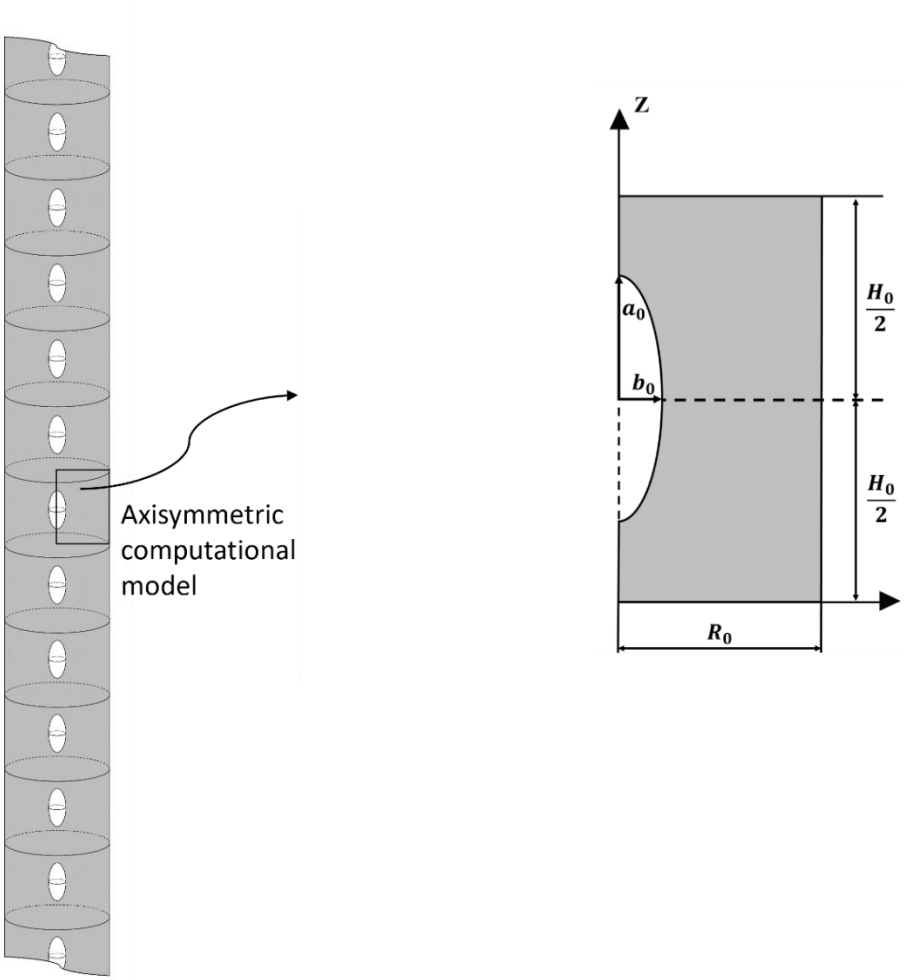

(a) (b)

Figure 1 (a) Schematic of a representative long cylindrical bar containing spheroidal voids homogeneously distributed along the center line of the bar. (b) Axisymmetric cylindrical RVE computational model.

To generate the mesoscale representative cylindrical bar, the RVE is repeated several times, in sequence, Fig.1a. The axisymmetric cylindrical RVE has micrometer length, H_0, radius, R_0, and contains a single spheroidal void symmetrically placed at the center such that the axis of

the RVE coincides with the Z-axis of the void, Fig.1b. The initial porosity of the RVE, f_0, is the same as those of the porous medium.

The spheroidal void has two length parameters, a_0 and b_0. The initial aspect ratio of the void is defined as:

$$\lambda_V = \frac{a_0}{b_0} \tag{1}$$

The void has spherical, oblate and prolate shapes when $\lambda_V = 1$, $\lambda_V < 1$ and $\lambda_V > 1$, respectively. For a given initial porosity f_0 and void dimensions a_0 and b_0, the initial length parameters of the unit cell are related by:

$$H_0 R_0^2 = \frac{4}{3}\frac{a_0 b_0^2}{f_0} \tag{2}$$

Several RVE models with various initial porosities and length parameters are generated to study the effect of the initial porosity, void size, and void shape on the shock structure profile, and to examine the micro-inertia effects. The effect of the spatial distribution of voids will be also analyzed by varying the aspect ratio of the cell:

$$\lambda_C = \frac{H_0}{2R_0} \tag{3}$$

2.2 Finite-Element Modeling

Because in plate impact experiments, the lateral dimensions of the plate are large, no displacements at the macroscopic level are allowed perpendicular to the impact direction. Thus, the radial displacement of the circumferential boundary of the representative cylindrical bar is set to zero. A constant axial velocity V_{imp} is imposed at the lower boundary of the target. This can be thought, for instance, as the result of the impact at the speed V_{imp} of a massive striker with very large impedance. Upon impact, elastic and plastic shockwaves are generated in the target initially at rest.

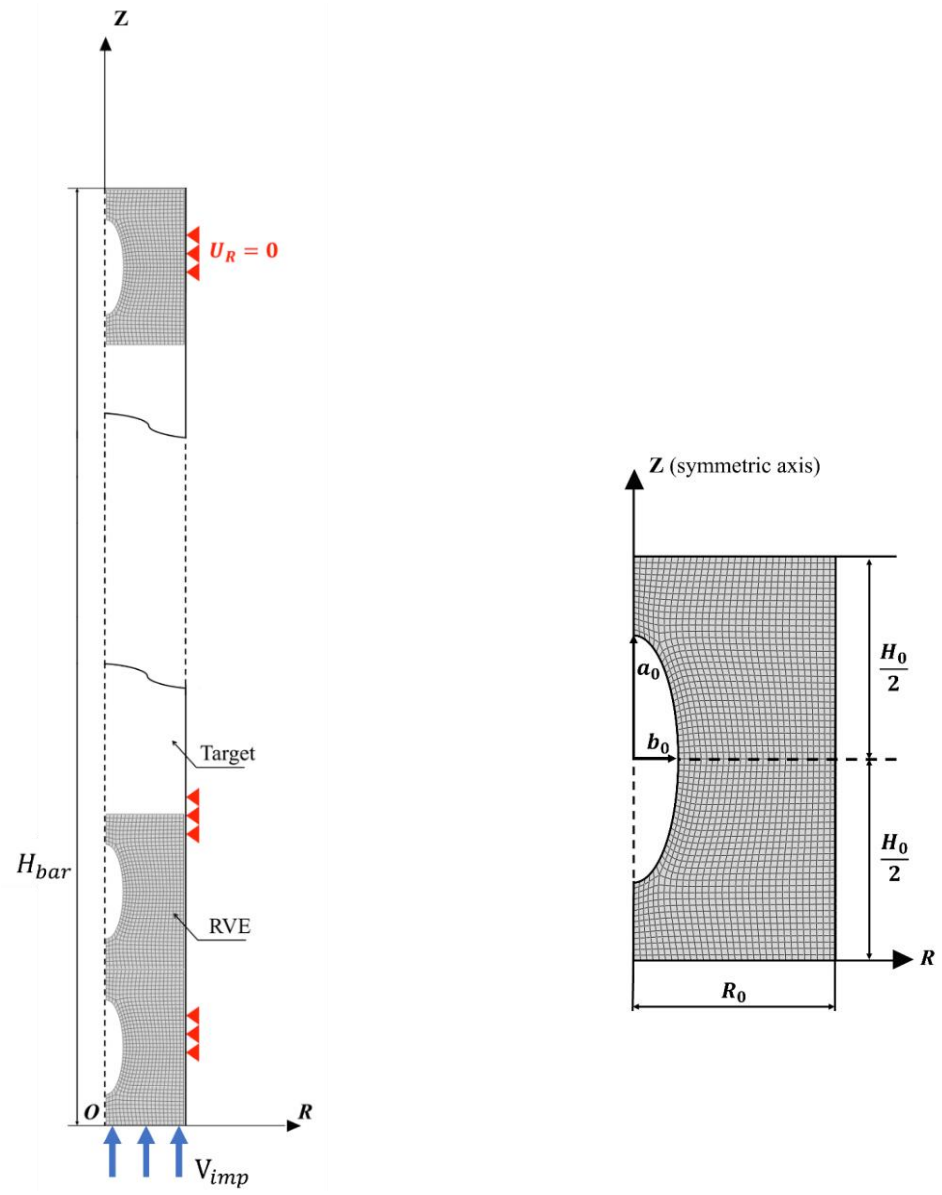

(a) (b)

Figure 2: (a) 2D axisymmetric cylindrical FE model: the target, a long porous cylindrical bar with initial spheroidal voids. An initial particle velocity V_{imp} is assigned at the extremity $Z = 0$ (b) Example of mesh density of a 2D axisymmetric RVE with f_0 =2%, $R_0 = H_0/2$, $H_0 = 317\mu m$ and $a_0 = 97\mu m$, $b_0 = 35\mu m$. Nominal size of finite elements $L_e = 7.5\mu m$.

Due to the large deformations encountered in shock experiments, geometrical nonlinearities are included in the calculation. It should be noted that at the surface of each void, an interaction of "self-contact" is assigned in the case that a full collapse of the void occurs. In addition, a rigid wall was positioned at a distance of 0.001µm from the Z-axis, and a "Surface-

to-surface contact" interaction (frictionless) was applied to the FE model surfaces with this rigid-wall surface to prevent nodes from crossing the Z-axis.

The bar, with length $H_{bar} \cong 11.5mm$, is long enough to (i) let the shockwave reach a state state and (ii) avoid the interaction of the wave reflected from the free-end surface with the plastic shockwave at the time of the analysis. For a given unit cell of length H_0, the number of voids in the Finite Element model of a cylindrical bar of length H_{bar}, is given by H_{bar}/H_0. The bar, with length $H_{bar} \cong 11.5mm$, is long enough to avoid the interaction of the waves reflected from the free-end surface with the shockwaves at the time of the analysis. The bar is discretized into 4-node axisymmetric elements with reduced integration and hourglass control (CAX4R, in Abaqus). An effective refined mesh density is used with approximate element size depending on the volume of the RVE. An example of mesh density and approximate element size for a RVE with 2% porosity and containing a spheroidal void is shown in Fig. 2b. It should be noted that a FE convergence study has been done to assess the appropriate mesh density that can provide an acceptable solution.

2.3 Constitutive Modeling

We consider that the matrix material is a ductile metal with a mechanical response described by the Cowper-Symonds law, Eq. (4), and the Mie-Grüneisen EOS, Eq. (5). The Cowper-Symonds model expresses the equivalent Mises flow stress, σ, in terms of strain hardening and strain-rate hardening in a multiplicative form:

$$\sigma(\varepsilon, \dot{\varepsilon}) = (A + B\varepsilon^n)\left[1 + \left(\frac{\dot{\varepsilon}}{D}\right)^{1/p}\right] \tag{4}$$

$\varepsilon = \int_0^t \dot{\varepsilon}(\tau)\mathrm{d}\tau$ is the accumulated plastic strain, $\dot{\varepsilon}$ the Mises equivalent plastic strain rate, A and B are tensile-strength parameters, n is the strain-hardening exponent, D a reference strain rate and $1/p$ the strain rate sensitivity exponent. Plastic flow is assumed to obey the Mises J_2-flow theory.

In this paper, the matrix is made up of dense aluminum. In addition, moderate shock pressures are considered, so that, in first approximation, the temperature effects are neglected. It was shown for dense aluminum [48] and for porous aluminum [10, 22] that experimental results could be well restituted under such assumptions.

Since the Cowper-Symonds model is a phenomenological equation, the parameters should be calibrated based on experimental data. This is the subject of a forthcoming section.

Equation of state is essential to describe the shock response of a material [47]. The high-pressure response of the dense matrix material is modeled using the Mie-Grüneisen equation as follows:

$$P = \frac{\rho_0 c_0^2 \eta}{(1 - s\eta)^2}\left(1 - \frac{\gamma_0 \eta}{2}\right) + \gamma_0 \rho_0 E_m \tag{5}$$

where P is the pressure, E_m the internal energy per unit mass and $\eta = 1 - \rho_0/\rho$ the nominal volumetric compressive strain, ρ_0 and ρ being the initial and current densities, respectively, see Abaqus user's manual [49]. The parameter γ_0 stands for the Grüneisen ratio while c_0 and s define the linear relationship between the plastic shock-velocity, U_s, and the particle-velocity behind the plastic shock, U_p, as follows: $U_s = c_0 + sU_p$.

3. Steady Plastic Shocks for Dense Aluminum

3.1 Shock Structures

Steady plastic shock profiles obtained by Johnson & Barker [51] from plate impact experiments on dense aluminum are used to calibrate the Cowper-Symonds material parameters, see Fig. 3. These shock profiles show the evolution of the particle velocity over time. The simulations are performed with values of the initial mass density ρ_0, the shear modulus, G, and the EOS parameters, (c_0, s, γ_0) taken from Meyers [47], see Table 1.

Aluminum 6061

Material parameters	*A* [MPa]	*B* [MPa]	*n*	*D* [s^{-1}]	*p*	*G* [GPa]
	330	660	0.65	10^7	2	26.1

EOS parameters	c_0 [m/s]	*s*	γ_0	ρ_0 [kg/m^3]
	5350	1.34	2	2700

Table 1: Cowper-Symonds material parameters, equation of state parameters, shear modulus, and density for aluminum 6061 used in the FE analyses. Note that in addition to the shear modulus the elastic bulk modulus K can be obtained from $K = \rho_0 c_0^2$.

For the strain rate sensitivity parameter involved in Eq. (4) a fixed value is adopted: $1/p = 0.5$. This value is chosen in accordance with the Swegle & Grady [51] scaling law relating the stress jump $\Delta\sigma$ to a measure, $\dot{\varepsilon}_{SG}$, of the strain rate within a plastic shock. A large variety of polycrystalline metals, including aluminum, were investigated and a universal exponent of four was found in a power-law relationship, $\dot{\varepsilon}_{SG} = F\Delta\sigma^4$, where F is a material dependent parameter. From these results, all tested materials exhibited the same strain rate sensitivity of $1/p = 0.5$ for the regime encountered in shock wave experiments, see also [10, 48, 52]. Cowper-Symonds parameters *A*, *B*, *n* and *D* reported in Table 1 are obtained from the calibration of the simulated steady shock-profiles (particle velocity histories at a node located on the symmetry axis, Z, about 5 mm from the surface where the velocity V_{imp} is imposed) with experimental measurements corresponding to $V_{imp} = 240\, m/s$ and $V_{imp} = 540\, m/s$, Fig. 3.

Some notes should be reported here. First, for the dense material, the regime of deformation is purely uniaxial, so that at any point the displacements in the lateral direction X and Y are equal to zero. Therefore, FE calculations can be also performed under plane strain conditions (in the XZ plane) and compared to the simulations with the axisymmetric configurations. It has been checked that identical results are obtained with both approaches. Second, the numerical profile of the particle velocity over time is measured in the region where a stationary plastic shockwave is propagating through the bar (more details about steady

shockwaves will be given in section 4.2). Third, because the plastic shockwave is steady, the corresponding profile in Fig. 3 can be shifted over time to meet the experimental profile. Fourth, because the shockwaves of the experiments and simulations are measured at different places along the targets, the arrival times of the elastic precursor are different.

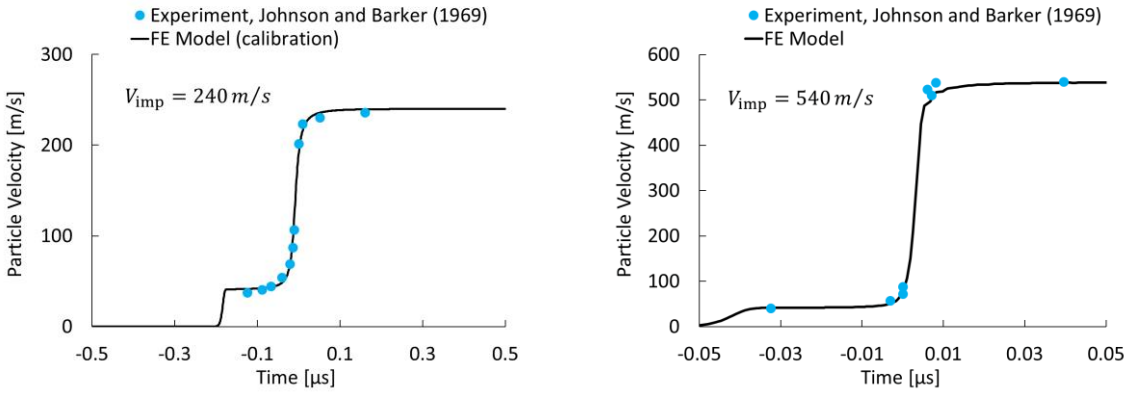

(a) (b)

Figure 3: Shock profiles showing the evolution of the particle velocity over time for imposed surface velocity (a) $V_{imp} = 240$ and (b) $540\,m/s$. The FE model results are compared with experimental data for dense aluminum obtained by Johnson and Barker [50].

Next, two additional shock profiles obtained from impact simulations of dense aluminum exposed to $V_{imp} = 325$, and $685\,m/s$, are plotted and compared to experimental profiles reported by Lovinger et al. [22]. The comparisons between the free surface-velocity profiles obtained in both experiments and simulations are shown in Fig. 4.

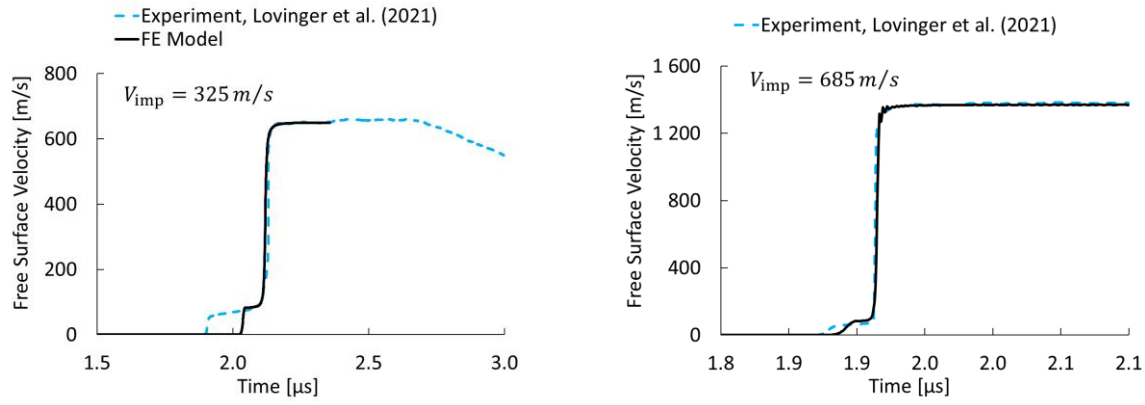

(a) (b)

Figure 4: Shock profiles showing the evolution of the free surface-velocity over time for imposed surface velocity (a) $V_{imp} = 325$ and (b) $685\,m/s$. The FE model results are compared with experimental data for dense aluminum obtained by Lovinger et al. [22]. Note that the experimental free surface velocity is compared to twice the particle velocity calculated at $Z = 5.03\,mm$.

Regarding FE predictions, the particle velocity is multiplied by two to obtain the free surface velocity, it is then shifted over time to meet the experimental steady plastic front. The experimental data are well reproduced by numerical predictions.

We should mention that higher values of elastic precursors are predicted by the FE model when compared to experimental results of Lovinger et al. [22], e.g., see Fig. 4a. This results from the identification of parameters from Fig. 3a where the elastic limit is not well defined. A better comparison would benefit from an adjustment of the material parameter A involved in Eq. (4), using the experimental free surface velocity of Lovinger et al. [22] at the Hugoniot elastic limit. However, it is verified that the plastic shock front is just slightly modified by such adjustment (see Supplementary Material).

Finally, it should be noted that the FE model together with the calibrated Cowper-Symonds parameters are validated in this study for analyses with a velocity range of $V_{imp} = 240 - 700\,m/s$. Later the validation will be extended to values of V_{imp} up to $900\,m/s$. The fitted Cowper-Symonds parameters given in Table 1 are fixed and used in all FE analyses performed in this study.

3.2 $U_s - U_p$ Diagram for Dense Aluminum

In this section, FE simulations are performed for dense aluminum subjected to V_{imp} ranging from 350 to $900\,m/s$. Plastic shock velocities, U_s, are calculated from the predicted shock profiles obtained at different points on the axis of symmetry at more than $5\,mm$ from the impact surface (further details on the characterization of U_s will be provided in subsection 4.2).

Fig. 5 shows ($U_s - U_p$) diagrams obtained experimentally, theoretically (from the relationship $U_s = c_0 + sU_p$ with parameters c_0 and s given in Table 1), and numerically.

Note that the values of U_p reported for finite element results correspond to the velocity V_{imp} assigned at the bottom nodes, see Fig.2a. First, one observes that numerical results slightly overestimate by about 1% the theoretical prediction of U_s. Despite this small deviation, the agreement between simulations, theoretical and experimental results shown in Fig. 5 provides validation of the FE analyses over the range $V_{imp} = 350 - 900\, m/s$.

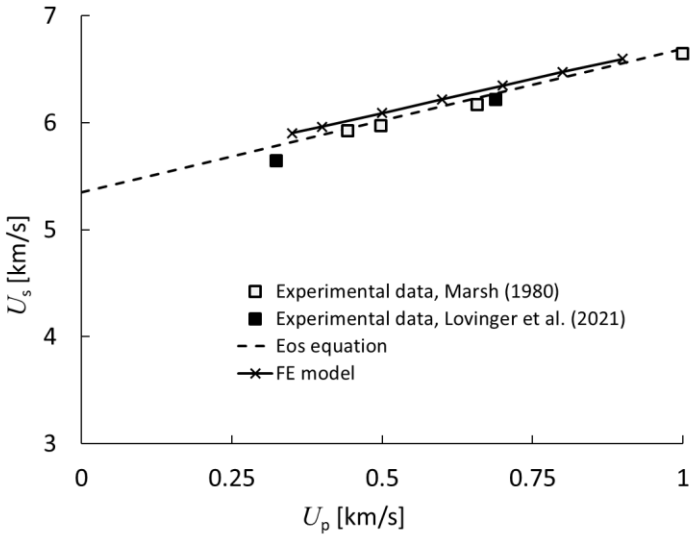

Figure 5: Plastic shock velocity U_s vs. particle velocity U_p at the rear of the plastic shock. Comparison of FE results against experimental data of Marsh [54] and Lovinger et al. [22] obtained for dense aluminum. The theoretical relationship $U_s = c_0 + sU_p$ is superimposed for the set of parameters $(c_0, s) = (5.35\,\mathrm{km/s}, 1.34)$ used as input in the numerical modeling.

It can be noted that a better fit between numerical results and experimental data could be reached by tuning the value of c_0 used as input parameter in the FE code (see Supplementary Material).

4. Steady Plastic Shocks in Porous Aluminum

Steady plastic shocks in porous aluminum are now analyzed. The effects on the shock structure of initial void size, void shape, spatial distribution of voids, porosity and imposed surface velocity are analyzed. The material parameters of the matrix are those reported in Table 1. We refer to the paper of Czarnota et al. [18] for an analytical approach of the effects of the material rate sensitivity on the shock profile. Here, the focus is made on the role of the void configuration and loading velocity.

4.1 Dimensional Analysis

A length, w, will be introduced to characterize the thickness of the core of the plastic shock front. A mean particle acceleration, $\bar{\gamma}_p$, characterizing the intensity of the acceleration sustained by a material particle within the core of the steady plastic shock will be also considered. For given velocity V_{imp} and initial porosity, it will be shown that $\bar{\gamma}_p$ is scaled by $1/w$. Therefore, the largest beneficial effect for plastic shock mitigation is obtained with a void configuration for which w is maximized.

The characteristic length w depends upon the initial configuration of pores through the void geometry a_0, b_0, and the spatial distribution of voids characterized in the present model by the cell geometry, H_0, R_0. There is also a dependence of w upon the material parameters listed in Table 1 and the velocity V_{imp}. A dimensional analysis provides the following relationship between dimensionless quantities:

$$\frac{w}{a_0} = \Phi_1\left(\frac{a_0}{b_0}, \frac{H_0}{a_0}, \frac{R_0}{a_0}, \frac{A}{\rho_0 V_{imp}^2}, \frac{B}{\rho_0 V_{imp}^2}, \frac{G}{\rho_0 V_{imp}^2}, \frac{D a_0}{V_{imp}}, \frac{c_0}{V_{imp}}, n, p, s, \gamma_0\right) \qquad (6)$$

By combining the arguments of the function Φ_1, the ratio w/a_0 can be written in terms of a function Φ_2:

$$\frac{w}{a_0} = \Phi_2\left(\frac{a_0}{b_0}, \frac{H_0}{2R_0}, f_0, \frac{A}{\rho_0 c_0^2}, \frac{B}{\rho_0 c_0^2}, \frac{G}{\rho_0 c_0^2}, \frac{D a_0}{V_{imp}}, \frac{c_0}{V_{imp}}, n, p, s, \gamma_0\right) \qquad (7)$$

We introduce the following notations:

$$\lambda_A = \frac{A}{\rho_0 c_0^2}$$

$$\lambda_B = \frac{B}{\rho_0 c_0^2}$$

$$\lambda_G = \frac{G}{\rho_0 c_0^2} \tag{8}$$

$$\lambda_D = \frac{D a_0}{V_{imp}}$$

$$\lambda_{c_0} = \frac{c_0}{V_{imp}}$$

By gathering the dimensionless material parameters that are not depending upon V_{imp}, into:

$$\chi = \left(\lambda_A, \lambda_B, \lambda_G, n, p, s, \gamma_0\right) \tag{9}$$

Eq. (7) can be written as:

$$\frac{w}{a_0} = \Phi\left(\lambda_V, \lambda_C, f_0, \lambda_D, \lambda_{c_0}, \chi\right) \tag{10}$$

where λ_V and λ_C are the aspect ratios defined by Eq. (1) and Eq. (3) and f_0 is the initial porosity.

Note that w/a_0 depends on the void configuration through: (i) the void morphology via λ_V, (ii) the void spatial distribution via λ_C, and (iii) the void size via λ_D. By increasing V_{imp}, $\lambda_D \to 0$ and the void size dependence becomes negligible in Φ. The shock width becomes also independent of the material rate sensitivity parameter D, and consequently, from Eq. (4), w becomes independent of the material parameter p. The characteristic length w appears to be scaled by a_0. Thus, denoting two homothetic initial configurations by $C = (a_0, b_0, H_0, R_0)$ and by $C_* = (a_0^*, b_0^*, H_0^*, R_0^*) = \alpha(a_0, b_0, H_0, R_0)$ with $\alpha > 0$, the corresponding shock widths are related by $w_* = \alpha w$, or $w_*/w = a_0^*/a_0$ (size effect on the plastic shock structure).

For spherical voids, the scaling of w by the void size a_0 at large impact velocities, and the negligible effect of the material rate sensitivity was demonstrated by Czarnota et al. [10, 18] by an analytical approach based on the numerical integration of evolution equations.

In the following, the morphological and topological effects resulting from void's configurations will be separately analyzed, by individually tuning the geometrical dimensionless parameters λ_V and λ_C involved in the function Φ.

Note that the dimensional analysis furnishes a functional relationship relating independent dimensionless parameters. However, one must highlight that the set of geometrical constraints ($b_0 < R_0$ and $2a_0 < H_0$) applies to the analysis. Using Eqs. (1, 3), this implies that the ratio λ_C/λ_V fulfills the following condition $2/(3f_0) > \lambda_C/\lambda_V > \sqrt{3f_0/2}$.

4.2 Steady Plastic Shocks Characteristics

To obtain from FE simulations the plastic shock-velocity, mean particle velocity behind the shock front, and plastic shock width, shock profiles are considered at different points (nodes) within the target. Shockwaves are portrayed here in terms of particle velocity histories.

The following notations are adopted: $V(\underline{\boldsymbol{X}}, t)$ denotes the particle velocity in the axial direction measured at time t and at the axisymmetric Lagrangian position $\underline{\boldsymbol{X}} = (R, Z)$, and $U_p(\underline{\boldsymbol{X}})$ is the time average value of $V(\underline{\boldsymbol{X}}, t)$ behind the plastic shock.

Particle velocities $V(\underline{\boldsymbol{X}}, t)$ are first measured at three Lagrangian positions $\underline{\boldsymbol{X}} = (R, Z)$ in a plane, $Z = constant$, at a mid-distance between two neighboring voids to show the consistency of the plastic shock profiles through this cross-section (henceforth denoted as mid cross-section). The measurement points are located at $Z = 5.16\ mm$, and at $0, R_0/2$, and R_0 in the radial direction (R). Fig. 6 shows the shock profiles for $V_{imp} = 350\ m/s$. The bar has initial porosity $f_0 = 2\%$, and contains spherical voids with $a_0 = b_0 = 20\mu m$, while the cell aspect ratio is $\lambda_C = H_0/2R_0 = 1$. From Eq. (2) these conditions imply that $H_0 = 128.7\mu m$.

As usually observed in elastic-plastic materials two compressive shockwaves are generated. The first shock is the elastic precursor which compresses the material to the elastic limit. It is followed by the plastic shock. The particle velocity behind the plastic shock is

oscillating around a mean value which stands for $U_p = V_{imp}$. Note that these oscillations, which are not observed with dense materials (e.g., see Fig. 3), find explanation in the presence of pores and vibrations at the cavities surface. Another observation from Fig. 6 is that the three profiles are practically identical. Thus, for most conditions considered here, the cross-section at the mid distance between two consecutive voids appears to remain planar after the passage of the plastic shock. Consequently, except otherwise specified, shock measurements on the symmetry axis are taken as representative of the response of the mid cross-section. However, this feature appears to be in default in some extreme cases, for instance when flow instabilities are activated at void surfaces (jet formation). This aspect will be further discussed in a forthcoming paper.

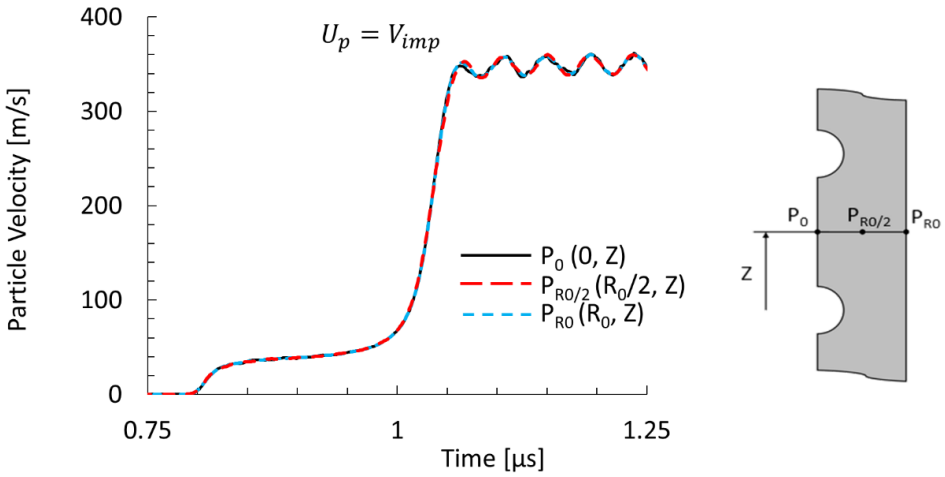

Figure. 6: Particle velocity vs. time profiles measured at three points in the radial direction for $V_{imp} = 350\ m/s$. The cell configuration is such that $\lambda_C = H_0/2R_0 = 1, H_0 = 128.7\mu m$, $\lambda_V = a_0/b_0 = 1$, $a_0 = 20\mu m$ (initial void radius) and $f_0 = 2\%$ (initial porosity). The measurement points are located at $Z = 5.16\ mm$.

Shock profiles are displayed in Fig. 7a at five different points P_i along the target axial axis to demonstrate that the plastic shock becomes steady (constant shape and speed) far enough from $Z = 0$ where V_{imp} is imposed. Each P_i is located at the mid distance between two consecutive voids. Times of arrival, $t(P_i)$, of the core of the plastic shock at P_i (i.e., when the

level of particle velocity reaches $U_p/2$ at point P_i) are reported in Fig.7a. We notify also the Lagrangian velocities of the plastic shockwave between consecutive points P_i and P_{i+1}:

$$U_s^{P_i \to P_{i+1}} = \frac{Z(P_{i+1}) - Z(P_i)}{t(P_{i+1}) - t(P_i)} \tag{11}$$

where $Z(P_i)$ is the Lagrangian axial position of P_i.

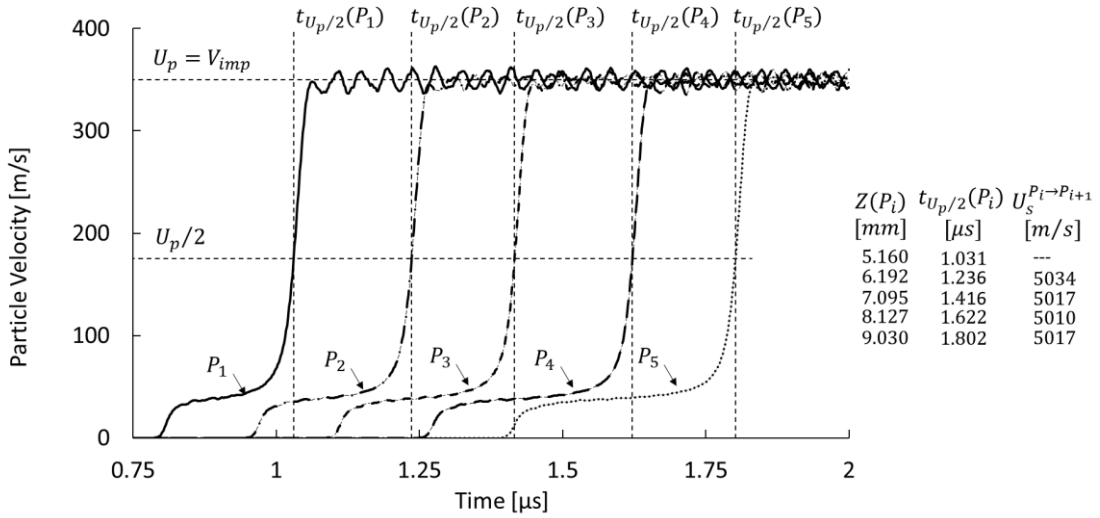

(a)

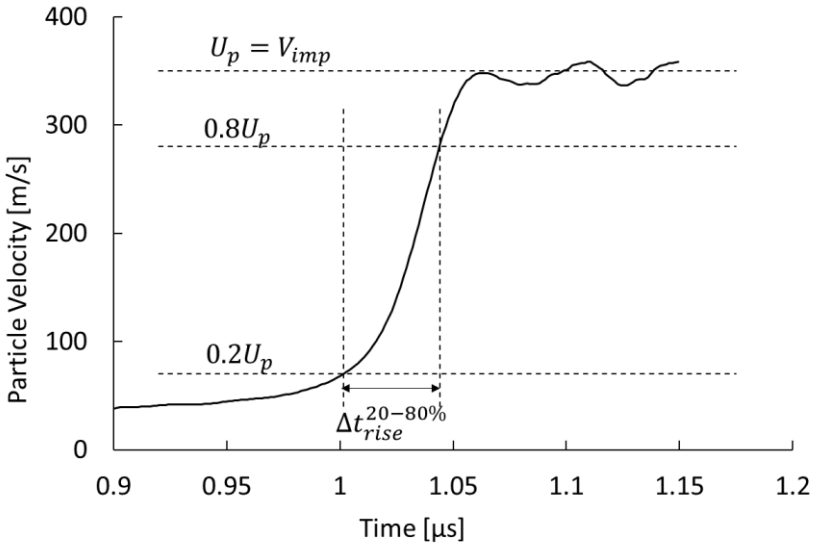

(b)

Figure. 7: Particle velocity vs time diagrams obtained for the same conditions as in Fig.6. (a) velocity histories at different locations P_i showing that the plastic shock is steady and

illustrating how the plastic shock velocity U_S is characterized. (b) definition of the rise time $\Delta t_{rise}^{20-80\%}$ from which the shock width, *w*, is characterized, see Eq. (12).

The small variations of $U_s^{P_i \to P_{i+1}}$ provide a first indication that the shock is steady. The plastic shock velocity, $U_s = 5020\, m/s$ is obtained by averaging the values of $U_s^{P_i \to P_{i+1}}$. Shock steadiness is further substantiated by the possibility to superimpose the shock profiles with time-shift.

In the following of the paper, plastic shock characteristics are obtained from shock structures at material points located on the bar axis, at the mid-distance between voids (at the initial time) and sufficiently far from $Z = 0$, where V_{imp} is imposed to get steady shocks.

A characterization of the width, w, of the core of the plastic shock layer is now introduced. From the plastic shock profile, we determine the rise time, $\Delta t_{rise}^{20-80\%}$, corresponding to the increasing ΔV of the particle velocity from $0.2\ U_p$ to $0.8\ U_p$ (20% to 80% of $U_p = V_{imp}$), see Fig. 7b. We have: $\Delta V = \beta U_p$ with $\beta = 0.6$. Then, the shock-width, w, and the average particle acceleration, $\bar{\gamma}_p$, are defined as follows:

$$w = U_s\, \Delta t_{rise}^{20-80\%} \tag{12}$$

$$\bar{\gamma}_p = \frac{\Delta V}{\Delta t_{rise}^{20-80\%}} = \frac{\beta U_p U_s}{w} \tag{13}$$

It will be shown that U_S depends on f_0 and U_p but not upon the void and cell aspect ratios, respectively λ_V and λ_C. Consequently, for given f_0 and $V_{imp} = U_p$, the mean particle acceleration $\bar{\gamma}_p$ is scaled by $1/w$. Thus, for shock mitigation the goal will be to optimize the void-configuration (i.e., shape and spatial distribution) in order to maximize w and attenuate the severity of particle acceleration according to Eq. (13).

5. Role of the Size, Shape, and Spatial Distribution of Voids

5.1 $U_s - U_p$ Diagram for Porous Aluminum

In all calculations, the set of matrix material parameters listed in Table 1 was fixed while many configurations have been tested by varying the void size and $\lambda_V, \lambda_C, f_0$ and by considering various velocities V_{imp}. The response of porous materials is known to be influenced by the shape of voids under static loading (e.g. [54-55]) while the additional effect of void size is involved under dynamic loading (e.g., see [10-12, 26-28]). For given V_{imp}, the dependence of the plastic shock structure upon porosity f_0 , void size and material parameters of the matrix material was analytically inferred for spherical voids by Czarnota et al. [10, 18]. Effects of void and cell aspect ratios, respectively λ_V and λ_C, are analyzed here.

Firstly, it is worth noting that the effects of void size, and of λ_V , λ_C on the plastic shock speed U_S were shown to be negligible in the range of tested configurations. Thus, U_S is solely depending on f_0 , material properties of the matrix and the velocity V_{imp}.

In fact, for the particular case of complete closure (full densification) of spherical voids, it was shown by Czarnota et al. [10] that the $U_s - U_p$ curve (for a given initial porosity) could be parametrized in terms of the shock stress level. In the case of full densification, this stress level depends solely upon material parameters of the dense material; consequently, for large enough impact velocities, the $U_s - U_p$ relationship does not depend upon the void size Interestingly, this result seems to remain valid even if the pores are or not completely closed and for non-spherical voids, as shown by the present numerical simulations.

Indeed, in the analytical approach of Czarnota et al. [18] there is a dependence of the plastic shock velocity upon the yield limit σ_e of the porous material and the corresponding stretch λ_e, see their Eq. (A15). The latter quantities are depending upon void shape and porosity, e.g. see [54-55]. From Eq. (A15), it can be seen that the influence of the void shape (through σ_e and λ_e) on the plastic shock speed becomes negligible when the shock stress is large enough. Moreover, in this case one can show that the shock speed is only depending on the initial

porosity, the matrix material properties, and V_{imp}. The same ideas apply to show that the spatial distribution of voids does not influence the speed of steady plastic shock when the impact velocity is sufficiently high. However, for very weak shocks, one expects an effect of the void shape and void spacing on the plastic shock speed.

We analyze the effect of relatively small initial porosities ($f_0 = 1, 2, 3, 4$ and 6%) on the $U_S - U_p$ relationship, by considering RVEs with $\lambda_C = 1$ and voids which are initially spherical ($\lambda_V = 1$) with radius, $a_0 = 20\mu m$. The following values of $V_{imp} = U_p$ are considered: 350, 400, 500, 600, 700, 800, and $900\, m/s$.

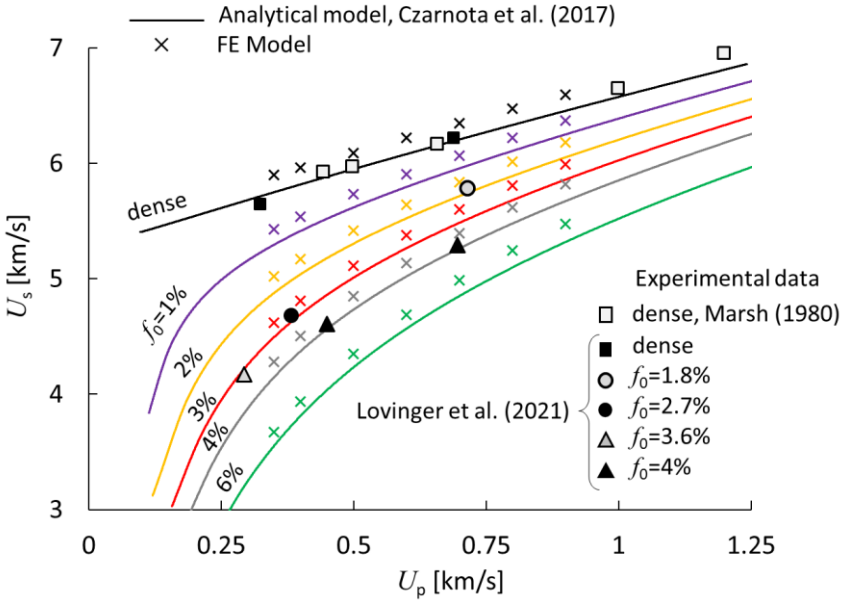

Figure 8: Plastic shock velocity U_s vs. particle velocity U_p behind the shock, for various values of the initial porosity f_0. FE simulations (crosses) are compared to experimental data for dense and porous aluminum obtained by Lovinger et al. [22]. Analytical results from Czarnota et al. [10], considering spherical voids, are also reported (solid lines). FE results are independent of the size and shape of voids and of the cell aspect ratio for the configurations and for the range of velocities V_{imp} $(= U_p)$ considered in this work.

Fig. 8 shows $U_s - U_p$ diagrams obtained from the FE simulations compared to the analytical model of Czarnota et al. [18] and to experimental data reported by Lovinger et al.

[22]. Good agreement can be seen between these results. In particular, an increase of the initial porosity leads to a decrease of the plastic shock velocity confirming common trends of the literature, e.g. [56]. As for the case of dense aluminum illustrated in Fig.5, one notes that FE calculations overestimate the shock velocity in porous aluminum. Here again, as mentioned in subsection 3.2, by tuning the value of c_0 used as input parameter, a better agreement between predicted, analytical, and experimental curves is achieved (see Supplementary material).

As previously stated, FE results reported in Fig.8 are anticipated to remain valid for any void size and for any void shape (λ_V) and cell aspect ratio (λ_C) in the range of cell configurations and of velocities V_{imp}considered in this work.

5.2 Spherical Voids with Quasi-Isotropic Spatial Distribution

In this section we consider spherical voids ($\lambda_V = 1$) and the cell aspect ratio is $\lambda_C = H_0/2R_0 = 1$ (quasi-isotropic spatial distribution of voids). The following parameters are varied: a_0, f_0 and V_{imp}; and numerical simulations are compared to experimental data. As stated in section 4.2, it is reminded that henceforth all shock characteristics are obtained for material particles located on the bar axis at the mid-distance between two consecutive voids.

Firstly, it was numerically verified in all cases considered here that there is no effect of void radius on the $U_s - U_p$ curves as previously reported in subsection 5.1.

In Fig. 9, free surface velocities are displayed in terms of time for two cases of initial void radii, respectively $a_0 = 20$ and $50\mu m$, corresponding to the range of pore sizes measured in the experiments reported by Lovinger et al. [22]. Each case is examined for the following experimental conditions: initial porosities, $f_0 = 2.7, 3.6, 4$, and 4.1%; imposed surface velocities of 404, 315, 700, and $460\ m/s$. The particle velocities are taken on the axial axis at $Z = 5\ mm$, multiplied by two and shifted over time to meet the reported experimental shock profiles measured at the free surface. In Fig. 9 the FE simulations are seen to be well correlated to the results obtained from the analytical model of Czarnota et al. [10, 18] and to the

experimental data of Lovinger et al. [22] over a range of initial porosities and imposed surface velocities V_{imp}. Micro-inertia effects related to the void size are clearly highlighted in the FE results, confirming the trends predicted by the analytical approach and observed as well in experiments. The small divergence between numerical and analytical models can be partly attributed to the differences in the material modeling of the matrix used in these models. One finally observes that higher elastic precursors are predicted by FE simulations. This feature was already noticed for dense aluminum (see Fig. 4a and b) and results from the value adopted for parameter *A* involved in Eq. (4). We refer to Supplementary Material where it is shown that the plastic shock structure is slightly affected by an adjustment of the value of the parameter *A*.

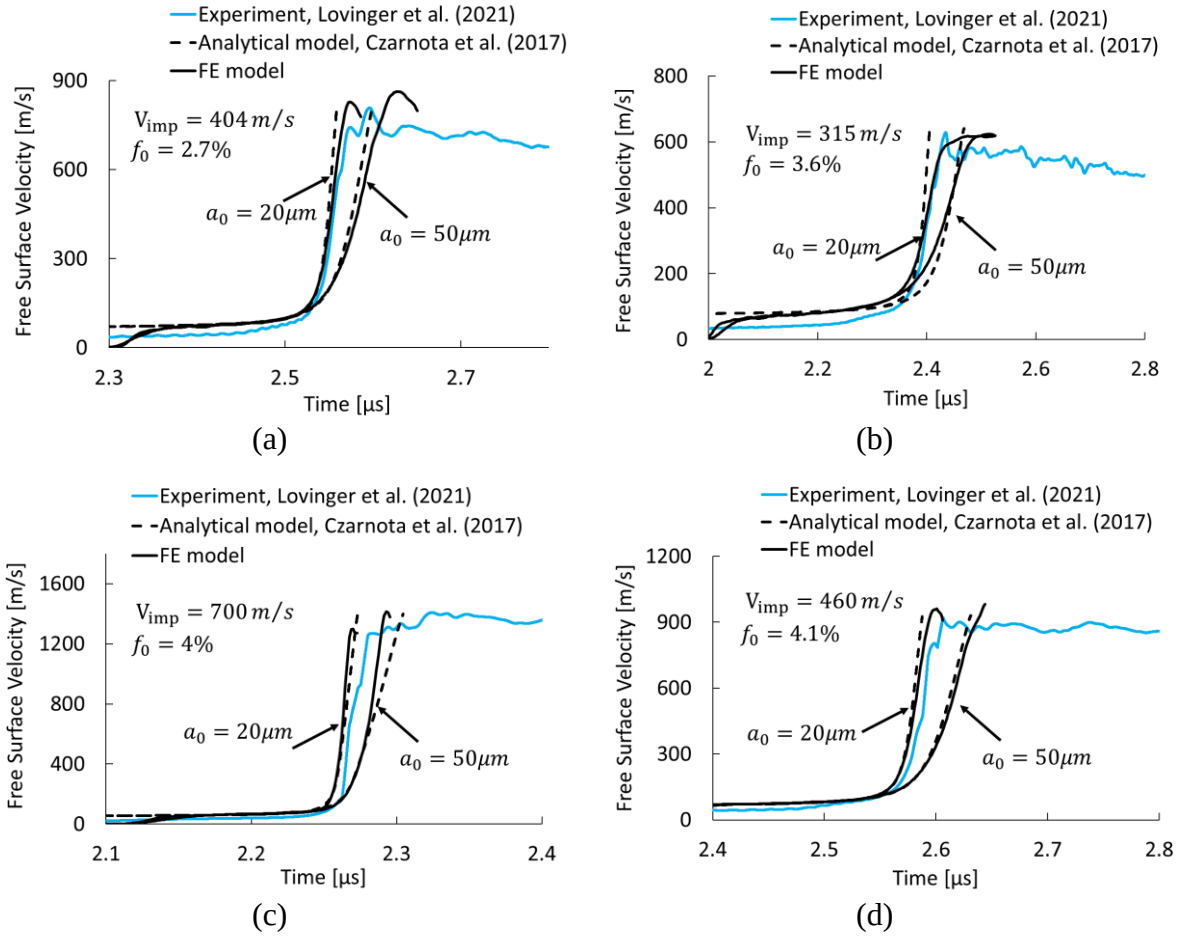

Figure 9: Shock profiles showing the evolution of the free surface-velocity over time for porous aluminum with an initial porosity of (a) 2.7, (b) 3.6, (c) 4, and (d) 4.1%, which is subjected to the imposed surface velocity of 404, 315, 700, and 460 m/s. The FE model

results are compared with analytical results of Czarnota et al. [10] (spherical voids of radius $a_0 = 20$ or $50\mu m$) and experimental data obtained by Lovinger et al. [22] for porous aluminum.

The effects of the imposed surface velocity, V_{imp}, and of the initial porosity, f_0, on the plastic shock width *w* are presented in Fig. 10 (see Table S1 in Supplementary Material for data). The initial pore radius is $a_0 = 20\mu m$. As predicted by the analytical approach proposed by Czarnota et al. [10], it is seen that for given V_{imp}, the shock width is increasing with f_0, while for given f_0, *w* is a decreasing function of V_{imp}.

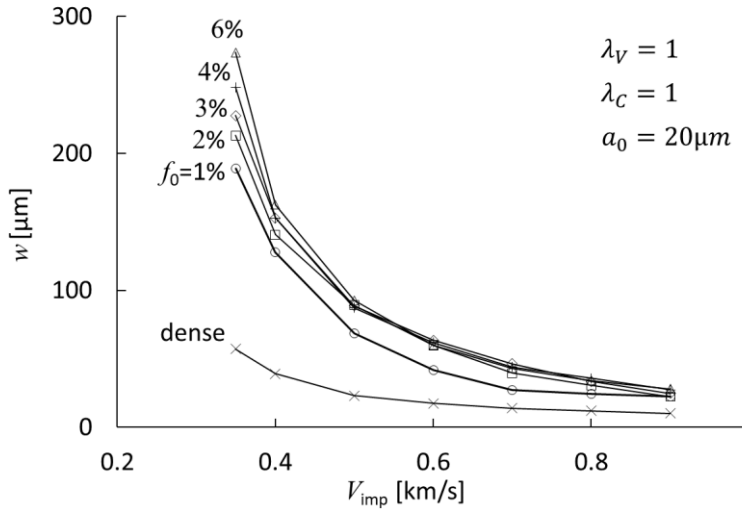

Figure 10: Plastic shock width *w* versus the imposed surface velocity, V_{imp}, for various values of the initial porosity, f_0. The voids are spherical ($\lambda_V = 1$) and the cell aspect ratio is $\lambda_C = 1$. The initial void radius is $a_0 = 20\mu m$. The bottom curve is for $f_0 = 0$ (dense aluminum).

In Fig. 11a, the effects on *w* of the initial void radius a_0 and of V_{imp} are investigated for the initial porosity, $f_0 = 2\%$. We refer to Supplementary Material, Table S2 for data. The width of the plastic shock appears to be increasing with the initial void size. Again, these results confirm the trends revealed by the theoretical approach of Czarnota et al. [10, 18]. In particular, it is seen that for sufficiently large values of V_{imp} ($\geq 500\ m/s$) and of a_0 ($\geq 30\mu m$), the plastic shock width is scaled by the void radius (equivalently, by the cell size since f_0 is fixed).

This scaling law is valid when the plastic shock is structured by micro-inertia effects with a negligible effect of the matrix rate dependence.

In Fig. 11b the mean particle acceleration $\bar{\gamma}_p$ given by Eq. (13) is displayed in terms of V_{imp} for two values of the void radius: $a_0 = 20$ and $50\mu m$. We have also calculated the maximum acceleration sustained by the material particle: $\gamma_p^{max} = \max_t(dV/dt)$. A good correlation is found in Fig. 11b between the variations of $\bar{\gamma}_p$ and of γ_p^{max} on the one hand, and the variation of the shock width in Fig. 11a on the other hand: as expected, the smaller is the shock width *w*, the larger are the accelerations $\bar{\gamma}_p$ and γ_p^{max}. Therefore, *w* can be viewed as a pertinent measure of the severity of the plastic shock.

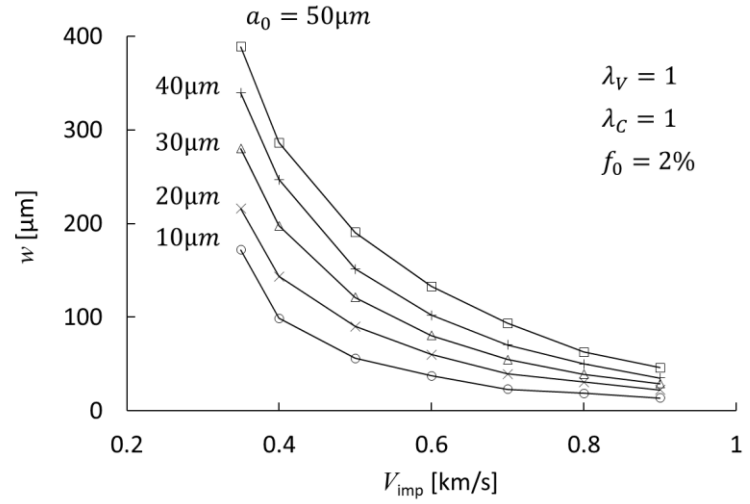

(a)

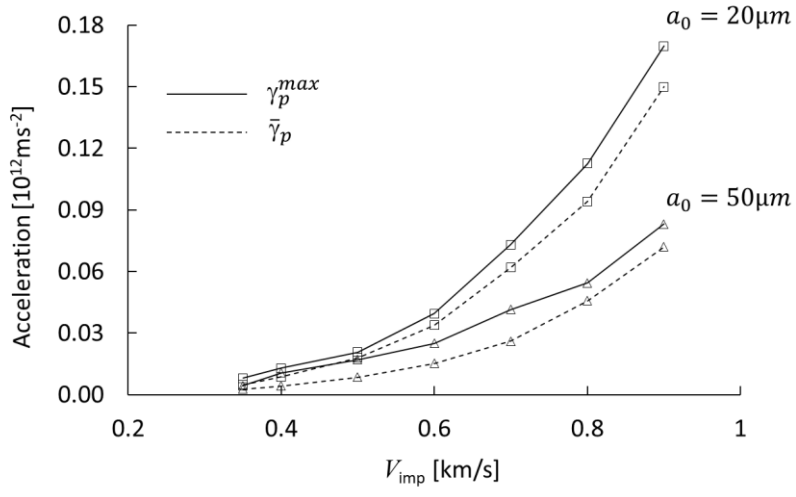

(b)

Figure 11: (a) Plastic shock width *w* versus the imposed surface velocity, V_{imp}, for spherical voids with different void radii: $a_0 = 10, 20, 30, 40$ and $50\mu m$. (b) Comparison between the maximum particle acceleration, γ_p^{max}, and the average particle acceleration, $\bar{\gamma}_p$, computed by Eq. (13) for spherical voids with radii $a_0 = 20$ and $50\mu m$. The cell aspect ratio is $\lambda_C = 1$ and the initial porosity is $f_0 = 2\%$.

5.3 Effect of the Void Shape on the Plastic Shock Structure

In this section we analyze the effect of the void aspect ratio, λ_V, on the shock structure. As reported in subsection 5.1, it has been verified that the FE simulations showed no effect of the void shape on the $U_s - U_p$ curve for the configurations examined in this section where the cell aspect ratio, the initial porosity and the axial void-length are fixed: $\lambda_C = 1$, $f_0 = 2\%$, $a_0 = 50\ \mu m$. For given V_{imp}, the dimensionless parameters other than λ_V in the function Φ of Eq. (10) are kept constant.

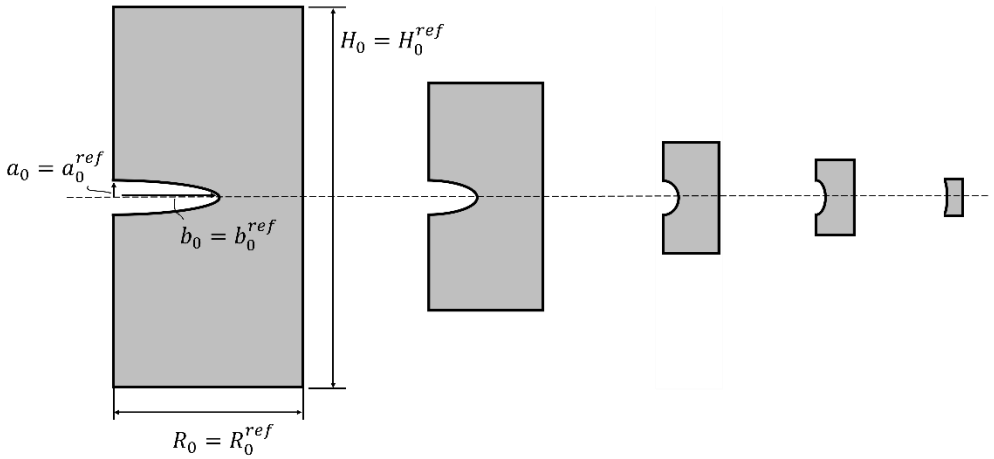

Figure 12: We consider unit cells with same aspect ratio $\lambda_C = H_0/2R_0 = 1$, initial porosity $f_0 = 2\%$, and $a_0 = 50\mu m$, and with variable void aspect ratio, $\lambda_V = a_0/b_0$. The reference cell is shown in (a) with $H_0^{ref} = 1063\mu m$, $R_0^{ref} = H_0/2$, $a_0^{ref} = 50\mu m$, $b_0^{ref} = 300\mu m$. Other cell configurations are defined from the reference cell as follows: $a_0 = a_0^{ref}$, $b_0 = \alpha_1 b_0^{ref}$, with $\alpha_1 > 0$. The cell size is varying according to $H_0 = {\alpha_1}^{2/3} H_0^{ref}$, $R_0 = {\alpha_1}^{2/3} R_0^{ref}$

We have: (a) $\lambda_V = 0.167$ ($\alpha_1 = 1$); (b) $\lambda_V = 0.342$ ($\alpha_1 = 0.487$); (c) $\lambda_V = 1$ ($\alpha_1 = 0.167$); (d) $\lambda_V = 1.852$ ($\alpha_1 = 0.09$); (e) $\lambda_V = 4.386$ ($\alpha_1 = 0.038$).

A reference cell is considered with: $H_0^{ref} = 1063\mu m$, $R_0^{ref} = H_0^{ref}/2$, $a_0^{ref} = 50\mu m$, $b_0^{ref} = 300\mu m$, such that $\lambda_V^{ref} \cong 0.167$. In Fig.12 other cell configurations with variable void aspect ratio $\lambda_V = a_0/b_0 = \lambda_V^{ref}/\alpha_1$ are defined from this reference cell as follows: $a_0 = a_0^{ref}$, $b_0 = \alpha_1 b_0^{ref}$, $H_0 = {\alpha_1}^{2/3} H_0^{ref}$, $R_0 = {\alpha_1}^{2/3} R_0^{ref}$. Note that α_1 must be in the range [0.029, 5.56] in order to satisfy both conditions $2a_0 < H_0$ and $H_0/2 > b_0$. In Fig.12 five cell configurations are displayed with their corresponding values of void aspect ratio and of α_1. Two additional cells (with $\lambda_V = 0.033$ and 0.056) are considered; they are not shown in Fig.12 because their sizes are too big.

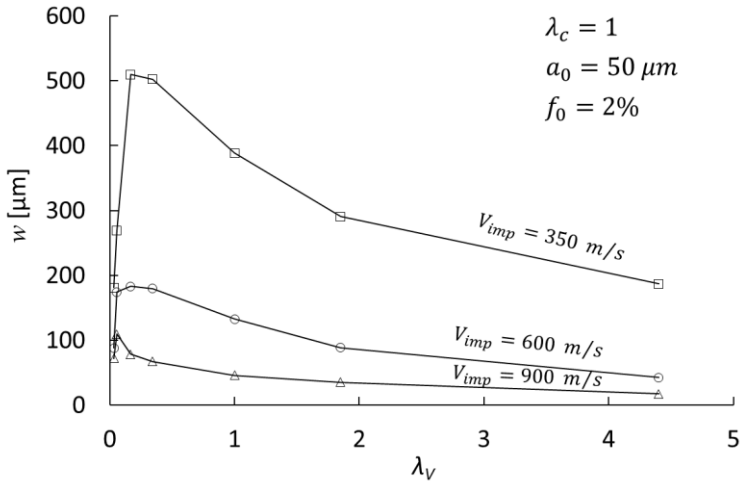

(a)

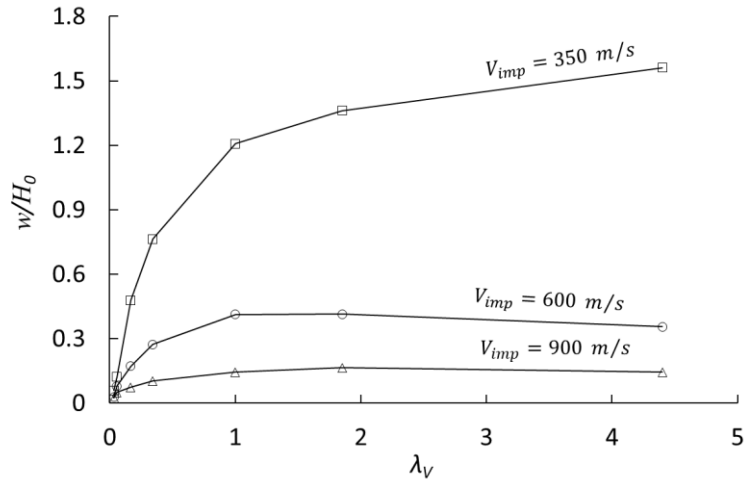

(b)

Figure 13: Effect of the void aspect ratio λ_V on the plastic shock width, *w*, for the imposed surface velocities $V_{imp} = 350, 600$ and 900 m/s, see Table S3 in Supplementary material. Cell configurations are those defined in Fig.12 and the additional cells with $\lambda_V = 0.033$ and 0.056. (a) *w* versus λ_V, (b) Normalized shock width w/H_0 versus λ_V.

Fig. 13a (resp. Fig. 13b) displays the shock width, *w*, (resp. the normalized width w/H_0) in terms of the void aspect ratio, λ_V, for $V_{imp} = 350$, 600 and 900 m/s. We refer to Table S3 in Supplementary material for data. The dependence of *w* upon λ_V appears in Fig.13a to be non-monotonic with important variations of *w*.

However, in Fig. 13b w/H_0 turns out to be mostly increasing (except for a slight decreasing at large λ_V for $V_{imp} = 600$ and 900 m/s). More precisely, two regimes can be distinguished in Fig. 13b. For $\lambda_V < 1$ (oblate voids) w/H_0 is rapidly increasing with λ_V. For $\lambda_V > 1$ (prolate voids) the variation of w/H_0 in terms of λ_V is either reduced (for $V_{imp} = 350 m/s$) or slightly negative (for $V_{imp} = 600$, and $900\ m/s$).

It is also interesting to observe in Fig.13b that: (i) except for very small λ_V, the shock width is in general of the order of the cell length H_0, (ii) the effect of V_{imp} on w/H_0 appears to be more important for prolate voids (large λ_V) than for oblate voids (small λ_V). Thus, microscale inertia effects can be viewed as being less operant for oblate voids.

The decreasing of w when λ_V is large for the cell configuration of Fig. 12, is related to the size effect which will be discussed in section 5.5, Fig.17.

5.4 Effect of the Spatial Distribution of Spherical Voids on the Plastic Shock Structure

The effect of the spatial distribution of voids (topological effect) can be indirectly simulated by varying the cell aspect ratio λ_C. As reported in subsection 5.1, it has been verified

that the FE simulations showed no effect of λ_C on the $U_s - U_p$ curve for the configurations examined in this section where spherical voids are considered with initial porosity $f_0 = 2\%$.

For given V_{imp} and fixed void radius a_0 the dimensionless parameters other than λ_C in the function Φ of Eq. (10) are kept constant. Thus, the intrinsic effect of the voids' topology can be inferred. This effect will be quantified for different values of V_{imp} and $a_0 = 20\mu m$. An additional case, $a_0 = 50\mu m$, is discussed in Supplementary material.

A reference cell is considered with $H_0^{ref} = 46.44\mu m$, $R_0^{ref} = 107.5\mu m$ (implying λ_C^{ref}=0.216) and $a_0^{ref} = b_0^{ref} = 20\mu m$, so that $f_0 = 2\%$. In Fig. 14 other cell configurations with variable aspect ratios $\lambda_C = H_0/2R_0 = \alpha_2^{3/2}\,\lambda_C^{ref}$ are defined from this reference cell as follows: $a_0 = a_0^{ref}$, $b_0 = b_0^{ref}$, $H_0 = \alpha_2 H_0^{ref}$, $R_0 = R_0^{ref}/\sqrt{\alpha_2}$. Thus, for all configurations of Fig.14 we have same initial void radius, cell volume and therefore same initial porosity.

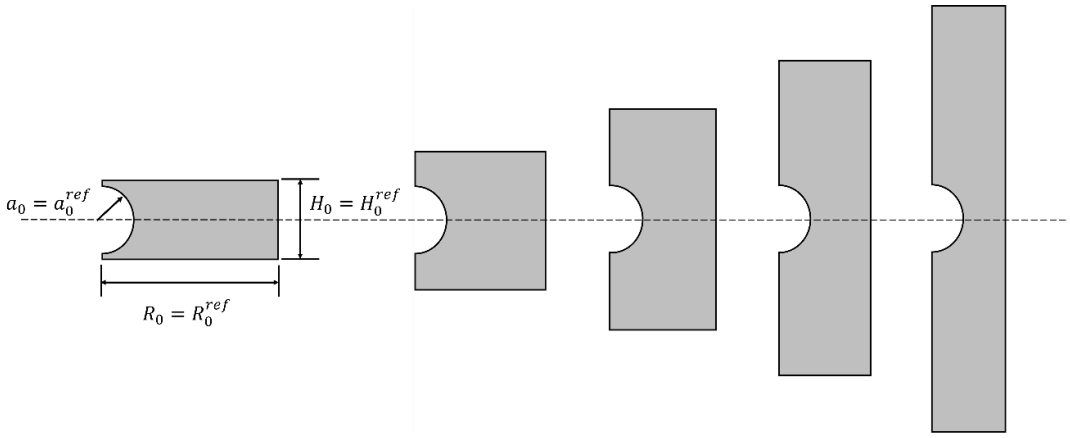

(a) (b) (c) (d) (e)

Figure 14: Unit cells with spherical void of same radius $a_0 = 20\mu m$ and porosity $f_0 = 2\%$ and with variable aspect ratio, $\lambda_C = H_0/2R_0$. The reference cell is shown in (a) with $H_0^{ref} = 46.44\mu m$, $R_0^{ref} = 107.5\mu m$. Other cell configurations are defined from the reference cell by $H_0 = \alpha_2 H_0^{ref}$, $R_0 = R_0^{ref}/\sqrt{\alpha_2}$ so that $\lambda_C = \alpha_2^{3/2}\,\lambda_C^{ref}$. We have: (a) $\alpha_2 = 1$ ($\lambda_c = 0.216$),- (b) $\alpha_2 = 1.78$ ($\lambda_C = 0.513$), (c) $\alpha_2 = 2.78$ ($\lambda_C = 1$), (d) $\alpha_2 = 4$ ($\lambda_C = 1.728$), and (e) $\alpha_2 = 5.44$ ($\lambda_C = 2.741$).

In some cases, the cross-section at the mid distance of two consecutive cells does not remain totally flat. Then, the measurement of the particle velocity at the center of the section is not representative of the response of other particles on the cell boundary. In particular, for $\lambda_C = 0.216$ and $V_{imp} = 900\, m/s$, a surface instability is triggered: a jet is formed at the void surface and pointed towards the void center in the wave propagation direction. A detailed analysis of void collapse mechanisms will be provided in a subsequent work allowing for a deeper understanding of the shock structure formation.

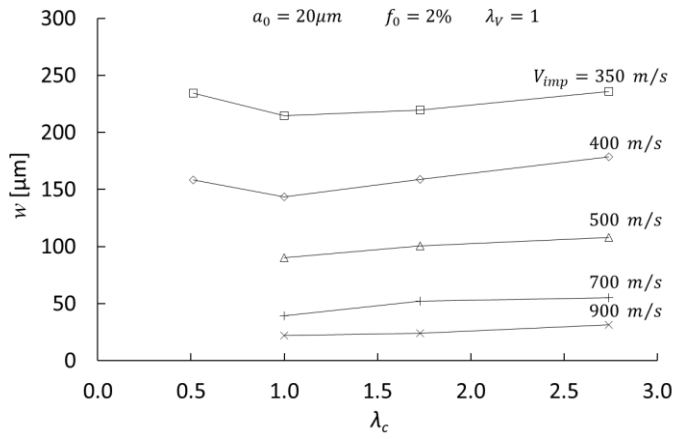

(a)

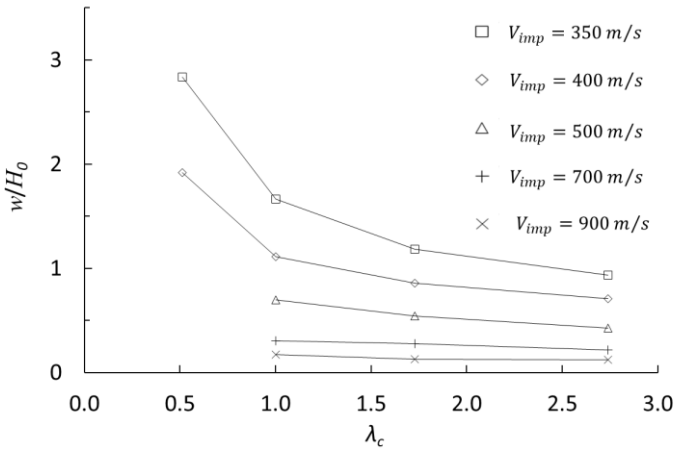

(b)

Figure 15: Effect of the cell aspect ratio λ_C and of V_{imp} on the plastic shock width, w. Cell configurations are those defined in Fig.14. Data are those of Table S4 provided in

Supplementary Material, with $a_0 = 20\mu m$. (a) w versus λ_C for various values of V_{imp}. (b) Normalized shock width w/H_0 versus λ_C.

Fig. 15a (resp. Fig. 15b) displays for various velocities V_{imp} the plastic shock width w (resp. w/H_0) in terms of the cell aspect ratio, λ_c for the void radius $a_0 = 20\mu m$. The trend is a weak increasing of w with λ_C, for $\lambda_C > 1$ and an important-decreasing of w/H_0, revealed for low velocities (V_{imp}=350 and 400m/s).

5.5 Effect of the Void Shape under Fixed Initial Cell Geometry and Fixed Initial Porosity

We consider now unit cells having same dimensions, $H_0 = 319\mu m$, and $R_0 = H_0/2$ ($\lambda_C = 1$). The void in the reference cell has the following characteristics: $a_0^{ref} = 15\mu m, b_0^{ref} = 90\mu m$. Other cell configurations are defined in Fig.16 by considering voids with same volume and different shapes: $a_0 = \alpha_3 a_0^{ref}$, $b_0 = b_0^{ref}/\sqrt{\alpha_3}$.

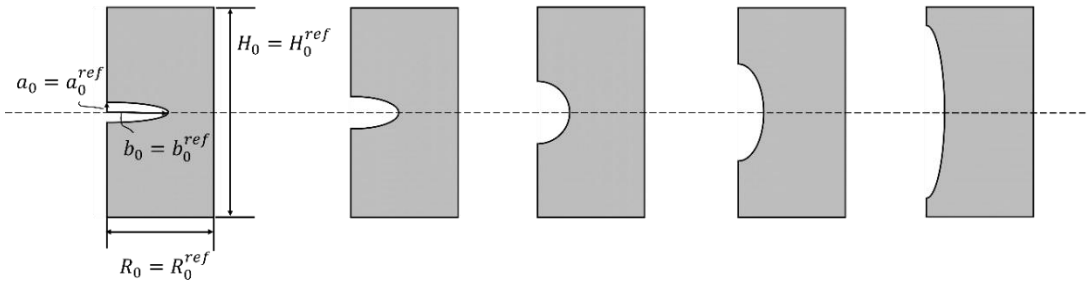

Figure 16: Unit cells with same dimensions $H_0 = 319\mu m$, and $R_0 = H_0/2$ ($\lambda_C = 1$). For the reference cell, the void characteristics are: $a_0^{ref} = 15\mu m$, $b_0^{ref} = 90\mu m$. Other cell configurations are defined by considering voids with same volume and different shapes: $a_0 = \alpha_3 a_0^{ref}$, $b_0 = b_0^{ref}/\sqrt{\alpha_3}$. The initial porosity is $f_0 = 2\%$ for all unit cells. We have: (a) $\alpha_3 = 1.6$ ($\lambda_V^{ref} = 0.167$), (b) $\alpha_3 = 1.6$ ($\lambda_V = 0.337$), (c) $\alpha_3 = 3.3$ ($\lambda_V = 1$), (d) $\alpha_3 = 4.9$ ($\lambda_V = 1.808$), and (e) $\alpha_3 = 8.8$ ($\lambda_V = 4.351$).

Thus, for all unit cells the initial porosity is $f_0 = 2\%$.

Eq. (10) can be written for all cells as:

$$\frac{w}{\alpha_3 a_0^{ref}} = F\left(\alpha_3{}^{3/2}\lambda_V^{ref}, \lambda_C, f_0, \alpha_3\lambda_D^{ref}, \lambda_{c_0}, \chi\right) \quad (14)$$

Therefore, both shape effect and void size effect (characterized by a_0) are involved in these simulations.

Here again, it has been verified with FE simulations that the same $U_s - U_p$ curves are obtained for all configurations of Fig. 16.

The plastic shock width is shown in Fig. 17a in terms of the void aspect ratio, λ_V, for $V_{imp} = 600\, m/s$, see also Table S5 in Supplementary Material. For the cell configurations of Fig. 16, the shock width gets its optimal value when the void is spherical ($\lambda_V = 1$). In Fig. 17a we have also reported the results of Fig. 13a for $V_{imp} = 600\, m/s$. Fig. 17b represents w/H_0 in terms of λ_V. For the two families of unit cells considered here, the values of w/H_0 are very similar, showing that the shock width is scaled by the cell size. It is interesting to compare the characteristics of the two families of unit cells, F^* and F^+ examined in Fig. 17b. The family F^* is defined in section 5.3 and illustrated in Fig. 12. F^+ is defined in section 5.5 and illustrated in Fig. 16. For both families we have $\lambda_C = 1$ and $f_0 = 2\%$.

The result of Fig. 17b can be analyzed from Eq. (10). For given V_{imp} and for given λ_V, λ_C and f_0, Eq. (10) indicates that the ratio w/a_0 is fixed (the dependence with respect to the term Da_0/V_{imp} becoming negligible but not those of c_0/V_{imp}), i.e. the shock width is scaled by the void length a_0.

This size effect was analyzed in Fig. 11 for spherical void. In Fig. 17b, the size effect is illustrated for any void shape. Results provided by Eq. (10) (w scaled by the void length a_0 for large V_{imp} are consistent with those shown in Fig. 17b (w scaled by the cell length H_0). Indeed, it can be easily demonstrated that cells of $F^*$and of F^+ are homothetic when they have same

void shape λ_V. The demonstration uses the fact that cell * and cell + have also same porosity f_0 and same aspect ratio λ_C. Consequently, for a given λ_V, it follows that:

$$\frac{a_0^*}{a_0^+} = \frac{H_0^*}{H_0^+} = \omega \tag{15}$$

where ω is a homothety ratio.

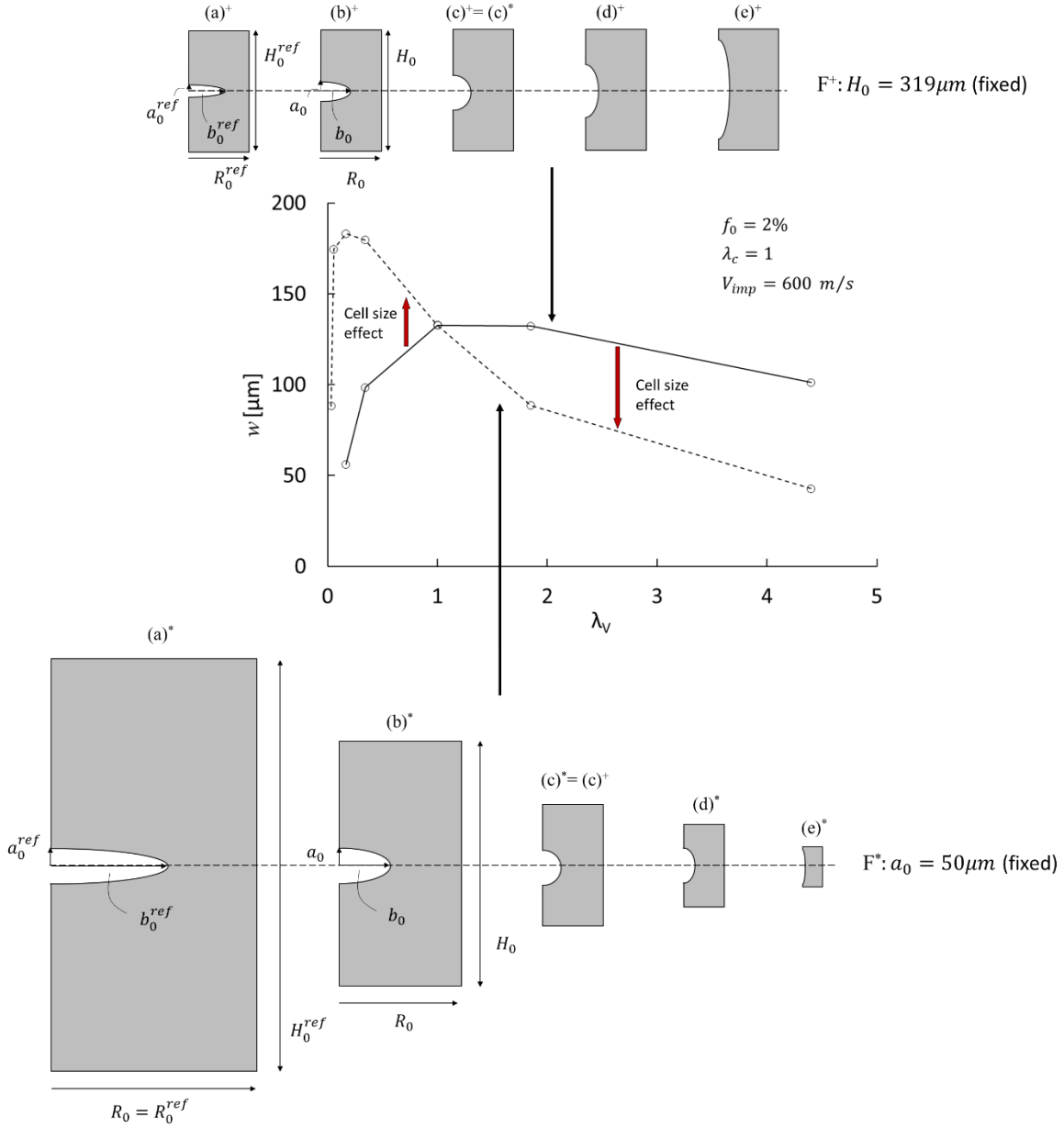

(a)

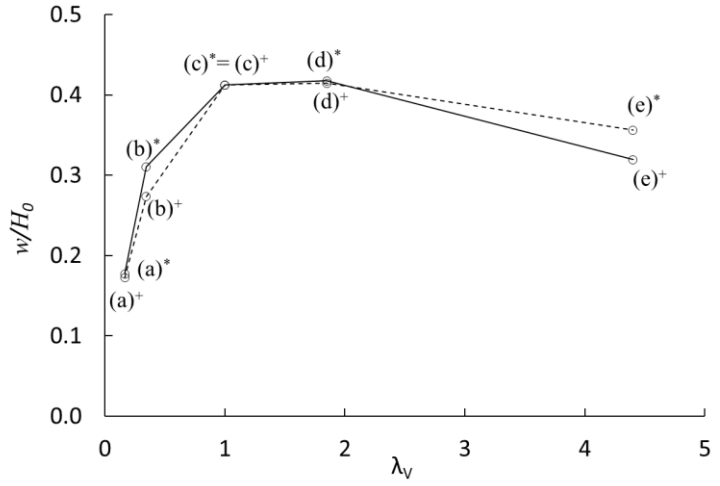

(b)

Figure 17: (a) Plastic shock width, *w*, with respect to the void aspect ratio $\lambda_V = a_0/b_0$ for the family F^* of unit cells defined in section 5.3 (and illustrated in Fig.12) and the family F^+ defined in section 5.5 (and illustrated in Fig.16). For both families we have $f_0 = 2\%$, $\lambda_C = 1$. The imposed surface velocity is $V_{imp} = 600\, m/s$. For the same λ_V the corresponding cells of F^* and of F^+ are homothetic. (b) w/H_0 versus λ_V. The shock width appears to be scaled by the cell size for homothetic cells (with same λ_V). For comparison, the plastic shock width for the dense material is $w_{dense} = 17.42\mu m$.

From Fig. 17b we have:

$$\frac{w^*}{H_0^*} = \frac{w^+}{H_0^+} \tag{16}$$

With Eqs. (15) and (16), we get:

$$\frac{w^*}{w^+} = \frac{H_0^*}{H_0^+} = \frac{a_0^*}{a_0^+} \tag{17}$$

Thus, *w* appears to be scaled equivalently by the cell length H_0 or by the void length a_0. In Fig.17a, for a given $\lambda_V < 1$, the cell * is larger than the corresponding cell + and the shock widths follow the same ordering: $w^* > w^+$. The reverse situation is observed for $\lambda_V > 1$ (cell * smaller than cell + and $w^* < w^+$). Cells are identical for $\lambda_V = 1$ and we have $w^* = w^+$. This

is a clear illustration of the size effect that occurs at high loading rates and this scaling is a consequence of micro-inertia effects, see [10].

Finally, Fig. 18a contains a synthetic presentation of the results obtained in subsections 5.2, 5.3 and 5.5 for the dependence of the plastic shock width w with respect to the void size (characterized by a_0) and the void aspect ratio λ_V, the initial porosity being, $f_0 = 2\%$, the cell aspect ratio, $\lambda_C = 1$ and the imposed velocity, $V_{imp} = 600\, m/s$. The general trends are: (i) an increasing of w with a_0 at constant λ_V. This is an illustration of the size effect for homothetic cells as discussed in Fig. 17; (ii) a non-monotonic evolution with λ_V at constant a_0. The values of w/H_0 and w/a_0 are also reported in Fig. 18b and c, respectively. For given λ_V it is seen that the shock width is scaled by the void size (for sufficiently large values of a_0 for which micro-inertia effects are quite significant), or by the cell size, the cells being homothetic.

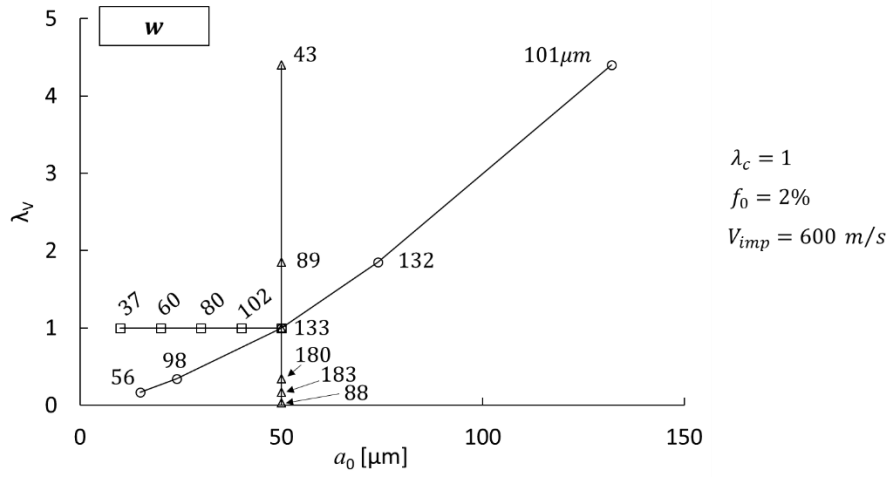

(a)

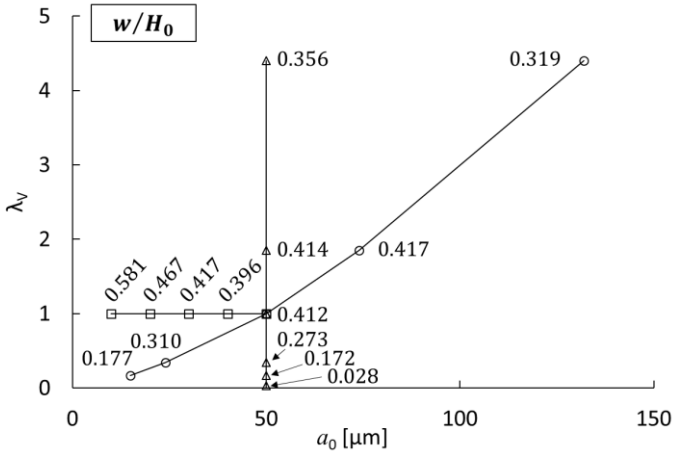

(b)

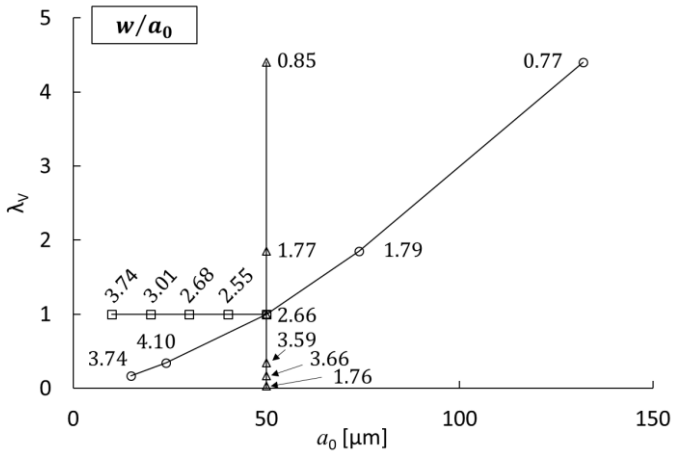

(c)

Figure 18: (a) Dependence of the plastic shock width, w, with respect to the void size a_0 and the void aspect ratio $\lambda_V = a_0/b_0$ and for $f_0 = 2\%$, $\lambda_C = 1$, $V_{imp} = 600\, m/s$. Values of (b) w/H_0 and of (c) w/a_0 are also shown to illustrate the size effect (w is scaled by the void length a_0 or equivalently by the cell length H_0 for given λ_V for sufficiently large values of a_0). Results are those reported in subsections 5.2 ($\lambda_V = 1$, a_0 varied), 5.3 ($\lambda_V$varied, $a_0 = 50\mu m$) and 5.5 ($\lambda_V$varied, a_0 varied).

6. Conclusion

Finite element simulations have been carried out to analyze steady plastic shock waves generated by planar impacts on porous metallic materials. The goal was to investigate, for various impact velocities, the effect of the void configuration on the plastic shock structure and propagation speed. The finite element model was constituted by a circular bar made up of a periodic pattern of identical unit cells. Identical spheroidal voids were located at the center of each unit cells in an axisymmetric configuration. Uniaxial deformation was imposed macroscopically in order to mimic the deformation mode encountered in plate impact experiments. The elastic-viscoplastic response of the matrix was described by a phenomenological Cowper-Symonds model and the high-pressure response by the Mie-Grüneisen equation of state.

The effects of cell size, cell aspect ratio, porosity, void aspect ratio and impact velocity on steady plastic shocks were investigated. The analysis was performed for porous aluminum with initial porosities between 0 and 6% and for imposed surface velocities up to 900 m/s.

The mains results are the following:

● for steady plastic shocks, the experimental shock velocity – particle velocity diagrams and the shock structures from literature are well restituted by the proposed finite element model.

● for the configurations considered in this paper, the plastic shock speed depends upon initial porosity and impact velocity but appears to be independent of the cell size and of the void and cell aspect ratios (the cell aspect ratio being a characteristic of the periodic void pattern).

● the effect of the void's configuration on the plastic shock width, *w*, was characterized for the fixed value of 2% of the initial porosity f_0. Effects of f_0 have been analyzed elsewhere [10, 18].

● for homothetic unit cells (i.e. initial configurations with same cell aspect ratio, same porosity, same void aspect ratio) the plastic shock width is proportional to the cell size when the impact velocity is sufficiently large (Fig.17). This is a manifestation of micro-inertia effects. This result generalizes to spheroidal voids, a similar finding previously obtained for spherical voids [10, 18].

● For given initial porosity, cell aspect ratio and cell size, the largest shock width is obtained for spherical voids or slightly prolate voids for the imposed surface velocity $V_{imp} = 600\ m/s$ (Fig17b). For $V_{imp} = 350\ m/s$ and $V_{imp} = 900\ m/s$, the largest values of *w* are realized with prolate voids, Fig.13b.

● the effect of the void aspect ratio on w/H_0 is reduced at large impact velocities, Fig.13b, H_0 being the cell length.

● for given initial porosity and given void size and aspect ratio, the sensitivity of *w* to the cell aspect ratio is slightly dependent on the impact velocity, Fig.15a. In general, the largest value of *w* is obtained for the largest axial void spacing (i.e. the smallest void lateral spacing), Fig.15a.

It has been shown that for given matrix rheological properties, given impact velocity and given initial porosity, shock mitigation can be significantly enhanced by tailoring the void configuration (void spacing, void shape, void size) in order to increase the plastic shock width. The larger is the shock width, the smaller is the acceleration of material particles and the less severe is the effect of the shock. Ultimately, one can think about using additive manufacturing to design an optimal void configuration for which the shock severity is minimum.

Some configurations (e.g. low cell aspect ratio) have revealed the activation of flow instabilities at the void surface. Further development of the numerical model would be to analyze the effect of size, shape, and spatial distribution of voids on collapse mechanisms. This is the subject of a forthcoming paper. In addition, an interesting aspect that emerges as a perspective in our current work is the analysis of the interplay between micro-inertia effects, coupled with geometric effects introduced by non-spherical voids, and the plastic anisotropy of the matrix material.

Aknowledgment

The authors thank the French State through the program "Investment in the future" operated by the National Research Agency (ANR) and referenced by ANR-11-LABX-0008-01 (LabEx DAMAS). C. Czarnota gratefully acknowledge the European Union's Horizon2020 Programme (Excellent Science, Marie-Sklodowska-Curie Actions) under REA grant agreement 777896 (Project QUANTIFY).

References

[1] Nesterenko, V.F., 2001. Dynamics of heterogeneous materials. Springer-Verlag, New York. https://doi.org/10.1007/978-1-4757-3524-6

[2] Gama, B. A., Bogetti, T. A., Fink, B. K., Yu, C.-J., Claar, T. D., Eifert, H. H., Gillespie Jr, J. W., 2001. Aluminum foam integral armor: a new dimension in armor design, *Composite Structures* (**52**) 3-4, 381-395.

[3] Destefanis, R., Schäfer, F., Lambert, M., Faraud, M., 2006. Selecting enhanced space debris shields for manned spacecraft, *International Journal of Impact Engineering* (**33**) 1-12, 219-230. https://doi.org/10.1016/j.ijimpeng.2006.09.065

[4] Smith B. H., Szyniszewski S., Hajjar J. F., Schafer B. W., Arwade S. R., 2012. Steel foam for structures: a review of applications, manufacturing and material properties. *Journal of Constructional Steel Research* (**71**), 1-10. https://doi.org/10.1016/j.jcsr.2011.10.028

[5] Jung, A., Lach, E., Diebels, S., 2014. New hybrid foam materials for impact protection, *International Journal of Impact Engineering* (**64**), 30-38. https://doi.org/10.1016/j.ijimpeng.2013.09.002

[6] Goel, M.D., Altenhofer, P., Matsagar, V.A., Gupta, A.K., Mundt, C., Marburg, S., 2015. Interaction of a shock wave with a closed cell aluminum metal foam. *Combustion, Explosion, and Shock Waves* (**51**), 373–380. https://doi.org/10.1134/S0010508215030144

[7] Winchester T., Kustra E., Cormier I., Cherniaev, A., 2023. Ballistic performance of integral body armor with closed-cell aluminum foam: A numerical study. *Forces in Mechanics* (**11**), 100187. https://doi.org/10.1016/j.finmec.2023.100187

[8] Wang, X., Li A., Liu, X., 2023. Fabrication of orientated micro porous metals: Control the melting process of powders by high scanning speed - ultra short hatch spacing scanning strategy, *Materials Letters* (**335**), 133741. https://doi.org/10.1016/j.matlet.2022.133741

[9] Al-Maharma, A. Y., Patil, S. P., Markert, B., 2020. Effects of porosity on the mechanical properties of additively manufactured components: a critical review, *Materials Research Express* (**7**) 12, 122001.

https://doi.org/10.1088/2053-1591/abcc5d

[10] Czarnota, C., Molinari, A., Mercier, S., 2017. The structure of steady shock waves in porous metals. *Journal of the Mechanics and Physics of Solids* (**107**), 204-228.

https://doi.org/10.1016/j.jmps.2017.06.005

[11] Czarnota, C., Jacques, N., Mercier, S., Molinari, A., 2008. Modelling of dynamic ductile fracture and application to the simulation of plate impact tests on tantalum. *Journal of the Mechanics and Physics of Solids* (**56**), 1624–1650.

https://doi.org/10.1016/j.jmps.2007.07.017

[12] Jacques, N., Czarnota, C., Mercier, S., Molinari, A., 2010. A micromechanical constitutive model for dynamic damage and fracture of ductile materials, *International Journal of Fracture* (**162**) 1, 159–175.

https://doi.org/10.1007/s10704-009-9436-2

[13] Versino, D., Bronkhorst, C., 2018. A computationally efficient ductile damage model accounting for nucleation and micro-inertia at high triaxialities. *Computer Methods in Applied Mechanics and Engineering* (**333**), 395–420.

https://doi.org/10.1016/j.cma.2018.01.028

[14] Qamar, S.B., Moore, J. A., Barton, N. R., 2022. A continuum damage approach to spallation and the role of microinertia. *Journal of Applied Physics* (**131**), 085901.

https://doi.org/10.1063/5.0078182

[15] Jacques, N., Mercier, S., Molinari, A., 2012. Effects of microscale inertia on dynamic ductile crack growth, *Journal of the Mechanics and Physics of Solids* (**60**), 665–690.

https://doi.org/10.1016/j.jmps.2011.12.010

[16] Jacques, N., Mercier, S., Molinari, A., 2015. A constitutive model for porous solids taking into account microscale inertia and progressive void nucleation, *Mechanics of Materials* (**80**), 311–323.

https://doi.org/10.1016/j.mechmat.2014.01.008

[17] Barthélémy, R., Jacques, N., Kerampran, S., Vermeersch, F., 2016. Modelling of micro-inertia effects in closed-cell foams with application to acoustic and shock wave propagation, *International Journal of Solids and Structures* (**97–98**), 445-457.

https://doi.org/10.1016/j.ijsolstr.2016.07.005

[18] Czarnota, C., Molinari, Mercier, S., 2020. Steady shock waves in porous metals: Viscosity and micro-inertia effects. *International Journal of Plasticity* (**135**), 102816.

https://doi.org/10.1016/j.ijplas.2020.102816

[19] Moore, J. A., Barton, N. R., 2022. A porosity-based model of dynamic compaction in under-dense materials. *International Journal of Solids and Structures* (**246–247**),111598.

https://doi.org/10.1016/j.ijsolstr.2022.111598

[20] dos Santos, T., Rodríguez-Martínez, J.A, 2021. Size effects on the plastic shock formation in steady-state cavity expansion in porous ductile materials. *Mechanics Research Communications* (**113**), 103690.

https://doi.org/10.1016/j.mechrescom.2021.103690

[21] Molinari, A., Mercier, S., 2001. Micromechanical modelling of porous materials under dynamic loading. *Journal of the Mechanics and Physics of Solids* (**49**), 1497–1516.

https://doi.org/10.1016/S0022-5096(01)00003-5

[22] Lovinger, Z., Czarnota, C., Ravindran, S., Molinari, A., Ravichandran, G., 2021. The role of micro-inertia on the shock structure in porous metals, *Journal of the Mechanics and Physics of Solids* (**154**), 104508.

https://doi.org/10.1016/j.jmps.2021.104508

[23] Nieto-Fuentes, J. C., Jacques, N., Marvi-Mashhadi, M., N'souglo, K. E., Rodríguez-Martínez, J. A., 2022. Modeling dynamic formability of porous ductile sheets subjected to biaxial stretching: Actual porosity versus homogenized porosity, *International Journal of Plasticity* (**158**) 103418.

https://doi.org/10.1016/j.ijplas.2022.103418

[24] Carroll, M.M., Holt, A.C., 1972. Static and dynamic pore collapse relations for ductile porous materials. *Journal of Applied Physics* (**43**), 1626–1636.

https://doi.org/10.1063/1.1661372

[25] Tong, W., Ravichandran, G., 1995. Inertial effects on void growth in porous viscoplastic materials. *Journal of Applied Mechanics* (**62**), 633–639.

https://doi.org/10.1115/1.2895993

[26] Sartori, C., Mercier, S., Jacques, N., Molinari, A., 2015. Constitutive behavior of porous ductile materials accounting for micro-inertia and void shape. *Mechanics of Materials* (**80**), 324–339.

https://doi.org/10.1016/j.mechmat.2013.12.006

[27] Sartori, C., Mercier, S., Jacques, N., Molinari, A., 2016. On the dynamic behavior of porous ductile solids containing spheroidal voids. *International Journal of Solids and Structures* (**97-98**), 150 – 167.

https://doi.org/10.1016/j.ijsolstr.2016.07.033

[28] Subramani, M., Czarnota, C., Mercier, S., Molinari, A., 2020. Dynamic response of ductile materials containing cylindrical voids. *International Journal of Fracture* (**222**), 197–218.

https://doi.org/10.1007/s10704-020-00441-7

[29] dos Santos, T., Nieto-Fuentes, J.C., Hosseini, N., Rodríguez-Martínez, J.A, 2022. The effect of voids shape on hypervelocity cylindrical cavity expansion and shock waves formation in transversely isotropic porous materials. *Acta Mechanica* (**233**), 1413–1434.

https://doi.org/10.1007/s00707-022-03172-z

[30] Monchiet, V., Cazacu, O., Charkaluk, E., Kondo, D., 2008. Macroscopic yield criteria for plastic anisotropic materials containing spheroidal voids. *International Journal of Plasticity* (**24**), 1158 – 1189.

https://doi.org/10.1016/j.ijplas.2007.08.008

[31] Zhao, F. P., Wu, H. A., Luo, S. N., 2013. Microstructure effects on shock response of Cu nanofoams. *Journal of Applied Physics* (**114**), 073501.

https://doi.org/10.1063/1.4818487

[32] Dávila, L. P., Erhart, P., Bringa, E. M., Meyers, M. A., Lubarda, V. A., Schneider, M. S., Becker, R., Kumar M., 2005. Atomistic modeling of shock-induced void collapse in copper. Applied Physics Letters (86), 16, 161902.

https://doi.org/10.1063/1.1906307

[33] Wood, M. A., Kittell, D. E., Yarrington, C. D., Thompson, A. P., 2018. Multiscale modeling of shock wave localization in porous energetic material, *Physical Review B* (**97**) 1, 014109.

https://doi.org/10.1103/PhysRevB.97.014109

[34] Chen, Z., Zhang X., Li, W., Yao, X., 2022. Shock compression of nanoporous silicon carbide at high strain rate. *International Journal of Mechanical Sciences* (**224**), 107320.

https://doi.org/10.1016/j.ijmecsci.2022.107320

[35] Song, W., Yu, Y., Guan, Y., 2022. Role of void shape on shock responses of nanoporous metallic glasses via molecular dynamics simulation, *International Journal of Mechanical Sciences* (**218**), 107076.

https://doi.org/10.1016/j.ijmecsci.2022.107076

[36] Sharma, A., Dubey, D. K., 2023. Effect of porosity on shock propagation behaviour of single crystal aluminium: A molecular dynamics investigation. *Mechanics of Materials* (**177**),104535.

https://doi.org/10.1016/j.mechmat.2022.104535

[37] Erhart, P., Bringa, E. M., Kumar, M., Albe, K., 2005. Atomistic mechanism of shock-induced void collapse in nanoporous metals, *Physical Review B* (**72**) 5, 052104.

https://doi/10.1103/PhysRevB.72.052104

[38] Wu, Z., Chen, X., Fu, T., Zheng, H., Zhao, Y., 2021. Molecular Dynamics Investigation of the Influence of Voids on the Impact Mechanical Behavior of NiTi Shape-Memory Alloy. *Materials* (**14**), 4020.

https://doi.org/10.3390/ma14144020

[39] Barton, N. R., Winter, N. W., Reaugh, J. E., 2009. Defect evolution and pore collapse in crystalline energetic materials. *Modelling and Simulation in Materials Science and Engineering* (17) 3, 035003.

https://dx.doi.org/10.1088/0965-0393/17/3/035003

[40] Austin, R. A., Barton, N. R., Reaugh, J. E. and Fried, L. E. 2015. Direct numerical simulation of shear localization and decomposition reactions in shock-loaded HMX crystal, *Journal of Applied Physics* (**117**) 18, 185902.

https://doi.org/10.1063/1.4918538

[41] Springer, H. K., Bastea, S., Nichols, A. L. III, Tarver, C. M., Reaugh, J. E., 2018. Modeling The Effects of Shock Pressure and Pore Morphology on Hot Spot Mechanisms in HMX. *Propellants, Explosives, Pyrotechnics* (**53**) 805 - 817.

https://doi.org/10.1002/prep.201800082

[42] Seshadri, P. K., Nguyen, Y. T., Sen, O., Udaykumar, H., S., 2022. Meso-scale simulation of energetic materials.II. Establishing structure–property linkages using synthetic microstructures. *Journal of Applied Physics* (**131**), 055905.
https://doi.org/10.1063/5.0065298

[43] Latypov, F. T., Fomin, E. V., Krasnikov, V. S., Mayer, A. E., 2022. Dynamic compaction of aluminum with nanopores of varied shape: MD simulations and machine-learning-based approximation of deformation behavior, *International Journal of Plasticity* (**156**), 103363.
https://doi.org/10.1016/j.ijplas.2022.103363

[44] Mayer, A. E., 2021. Micromechanical model of nanoparticle compaction and shock waves in metal powders International Journal of Plasticity (**147**), 103102.
https://doi.org/10.1016/j.ijplas.2021.103102

[45] Vishnu, A.R., Marvi-Mashhadi, M., Nieto-Fuentes, J.C., Rodríguez-Martínez, J.A., 2022a. New insights into the role of porous microstructure on dynamic shear localization. *International Journal of Plasticity* (**148**), 103150.
https://doi.org/10.1016/j.ijplas.2021.103150

[46] Cowper, G., Symonds, P., 1957. Strain hardening and strain-rate effects in the impact loading of cantilever beams, Technical rept. no. 28, Brown University Providence, R. I.

[47] Meyers, M.A., 1994. Dynamic Behavior of Materials. John Wiley & Sons, New York.
https://doi.org/10.1002/9780470172278

[48] Molinari, A., Ravichandran, G., 2004. Fundamental structure of steady plastic shock waves in metals. *Journal of Applied Physics* (**95**), 1718–1732.
https://doi.org/10.1063/1.1640452

[49] ABAQUS/Explicit, 2016. Abaqus Explicit v6.16 User's Manual. version 6.16 ed., ABAQUS Inc., Richmond,USA.

[50] Johnson, J. N., Barker, L. M., 1969. Dislocation Dynamics and Steady Plastic Wave Profiles in 6061-T6 Aluminum, *Journal of Applied Physics* (**40**), 4321-4334. https://doi.org/10.1063/1.1657194

[51] Swegle, J. W., Grady, D. E., 1985. Shock viscosity and the prediction of shock wave rise times. *Journal of Applied Physics* (**58**), 692–701. https://doi.org/10.1063/1.336184

[52] Kettenbeil, C., Lovinger, Z., Jiao, T., Mello, M., Clifton, R.J., Ravichandran, G., 2022. Inelastic behavior of tungsten carbide at high pressures, *Journal of the Mechanics and Physics of Solids* (**159**), 104762. https://doi.org/10.1016/j.jmps.2021.104762

[53] Marsh, S., 1980. LASL shock Hugoniot data. Los Alamos Scientific Laboratory Series on Dynamic Material Properties, Vol 5. University of California Press.

[54] Gologanu, M., Leblond, J.-B., Devaux, J., 1993. Approximate models for ductile metals containing non-spherical voids - case of axisymmetric prolate ellipsoidal cavities. *Journal of the Mechanics and Physics of Solids* (**41**), 1723–1754. https://doi.org/10.1016/0022-5096(93)90029-F

[55] Gologanu, M., Leblond, J.-B., Devaux, J., 1994. Approximate models for ductile metals containing non-spherical voids - case of axisymmetric oblate ellipsoidal cavities. *Journal of Engineering Materials and Technology* (**116**), 290–297. https://doi.org/10.1115/1.2904290

[56] Cohen, T., Durban, D., 2015. Steady shock waves in porous plastic solids. *International Journal of Solids and Structures* (**71**), 70–78. https://doi.org/10.1016/j.ijsolstr.2015.06.002